Monthly Notices
of the
ROYAL ASTRONOMICAL SOCIETY

MNRAS **503,** 5329–5350 (2021)
Advance Access publication 2021 February 26

doi:10.1093/mnras/stab527

Integral field spectroscopy of luminous infrared main-sequence galaxies at cosmic noon

L. Hogan,[1]★† D. Rigopoulou,[1] G. E. Magdis,[2,3,4,5] M. Pereira-Santaella,[1,6] I. García-Bernete,[1] N. Thatte,[1] K. Grisdale[1] and J.-S. Huang[7]

[1]*Department of Physics, University of Oxford, Keble Road, Oxford OX1 3RH, UK*
[2]*Cosmic Dawn Center (DAWN), University of Copenhagen, Jagtvej 128, Tårn I , 2200 Copenhagen N, Denmark*
[3]*DTU-Space, Technical University of Denmark, Elektrovej 327, DK-2800 Kgs. Lyngby, Denmark*
[4]*University of Copenhagen, Lyngbyvej 2, DK-2100 Copenhagen Ø, Denmark*
[5]*Institute for Astronomy, Astrophysics, Space Applications and Remote Sensing, National Observatory of Athens, GR-15236 Athens, Greece*
[6]*Centro de Astrobiología (CSIC-INTA), Ctra. de Ajalvir, Km 4, E-28850 Torrejón de Ardoz, Madrid, Spain*
[7]*National Astronomical Observatories, Chinese Academy of Sciences, Beijing 100012, China*

Accepted 2021 February 19. Received 2021 February 11; in original form 2020 September 17

ABSTRACT

We present the results of an integral field spectroscopy survey of a sample of dusty (ultra) luminous infrared galaxies (U/LIRGs) at $2 < z < 2.5$ using KMOS on the Very Large Telescope. The sample has been drawn from Herschel deep field surveys and benefits from ancillary multiwavelength data. Our goal is to investigate the physical characteristics, kinematics, and the drivers of star formation in the galaxies whose contribution dominates the peak of the cosmic star formation density. Two-thirds of the sample are main-sequence galaxies in contrast to the starburst nature of local U/LIRGs. Our kinematic study, unique in its focus on $z \sim 2$ dusty star-forming galaxies, uses the Hα emission line to find that ∼40 per cent appear to be isolated discs based on the ratio of rotational velocity to the velocity dispersion, suggesting steady-state mechanisms are sufficient to power the large star formation rates (SFRs). The ratio of obscured to unobscured star formation indicates the sample of galaxies experiences less dust obscuration compared to intermediate and local counterparts, while also hosting cooler dust than local U/LIRGs. In addition to Hα we detect [N II] 6583 Å in our targets and show the gas-phase metallicities do not exhibit the metal deficiency of local U/LIRGs. These results indicate that, despite their extreme IR luminosity, the underlying mechanisms driving the massive SFRs found at cosmic noon are due to scaled up disc galaxies as opposed to mergers.

Key words: ISM: kinematics and dynamics – infrared: galaxies – infrared: ISM; galaxies: ISM.

1 INTRODUCTION

(Ultra) Luminous infrared galaxies (U/LIRGs) are amongst the most powerful star-forming galaxies in the Universe. Their infrared (IR) luminosities arise from dust heated by newly formed massive stars and active galactic nuclei (AGNs), with AGNs being more prevalent and powerful with increasing luminosity. They are defined by their bolometric infrared luminosity and classified as: LIRGs $= 10^{11} < L_{IR} \equiv L_{8-1000\ \mu m} < 10^{12}\ L_{\odot}$ and ULIRGs $= 10^{12} < L_{IR} < 10^{13}\ L_{\odot}$ (Sanders & Mirabel 1996). These galaxies have large star formation rates (SFRs) ranging from tens up to thousands of solar masses per year (e.g. Rigopoulou, Lawrence & Rowan-Robinson 1996) Although relatively rare in the localU niverse, research has shown that their co-moving density increases by a factor of ∼ 1000 between redshifts of 1 and 2, where they are responsible for as much as 50 per cent of the star formation rate density (SFRD) (e.g. Magnelli et al. 2011; Murphy et al. 2011a). It has also been found that the cosmic SFRD gradually rises from $z = 8$ to peak around $z \approx 2$, known as cosmic noon, and then declines by an order of magnitude to the current epoch (e.g. Madau & Dickinson 2014). To understand the underlying mechanisms driving these large SFRs, we need to understand how U/LIRGs at this epoch form their stars.

In the past couple of decades multiwavelength studies have provided much insight into star formation and its interplay with gas, dust, and existing stellar mass. Observations have found a tight correlation between the SFR and stellar mass ($M_{\star}$) of a galaxy, known as the main sequence (MS) of star-forming galaxies (e.g. Daddi et al. 2007; Noeske et al. 2007). From this relation the specific SFR (sSFR $=$ SFR/$M_{\star}$) is defined, which can be viewed as the fractional growth of the stellar mass within a galaxy. The MS and sSFR can be used to categorize two populations of star-forming galaxies: steady-state secularly evolving galaxies fuelled from continuous in-falling gas from the intergalactic medium (e.g. Dekel, Sari & Ceverino 2009) and short-lived starbursts, which are periods of heightened star formation driven by mergers (e.g. Tacconi et al. 2008; Daddi et al.

★ E-mail: laurence.hogan@physics.ox.ac.uk
† Present address: Department of Physics, University of Oxford, Keble Road, Oxford OX1 3RH, UK

2010b; Genzel et al. 2010). Secular star-forming galaxies lie within a scatter of 0.3 dex of the MS, whereas starbursts fall in the region above, often defined as galaxies whose SFR is a factor of 4 or more above the MS correlation (e.g. Whitaker et al. 2012). As would be expected from the evolution of the cosmic SFRD the normalization of the correlation increases with redshift, i.e. for a given stellar mass the SFR of an MS galaxy at $z = 2$ is ∼20 times greater than an MS galaxy at $z = 0$ (e.g. Speagle et al. 2014), so secular evolving galaxies at high-z can have SFRs greatly exceeding local starbursts. A similar scaling relation exists between the gas within a galaxy and the SFR, known as the Kennicutt–Schmidtt law (Schmidt 1959; Kennicutt 1998). This correlation gives the star formation efficiency (SFE) of galaxies, i.e. how quick a galaxy can convert the molecular gas reservoirs into stars, and is one of the main mechanisms that determines a galaxies distance from the MS (e.g. Tacconi, Genzel & Sternberg 2020). As in the SFR-stellar mass plane, the Kennicutt–Schmidtt law is bimodal with starbursts appearing to have a higher SFE per stellar mass than MS galaxies (e.g. Daddi et al. 2010b).

Locally ($z < 0.2$) ULIRGs appear to be undergoing a transient starburst phase, fuelled by interactions and mergers, with a more diverse range of morphological types, such as isolated discs and minor mergers, appearing as the luminosity decreases down to the lowest luminosity LIRGs, which are dominated by secular processes (e.g. Bellocchi, Arribas & Colina 2016; Larson et al. 2016). Their IR spectral energy distributions (SED) are dominated by thermal emission from dust and have dust temperatures in the range 30–55 K (Clements et al. 2018 and references therein). They are very efficient at converting their molecular gas into stars (e.g. Gao & Solomon 2004) with depletion times ($\tau_{\rm dep} \equiv 1/{\rm SFE}$) of the order of 150 Myr (e.g. Elbaz et al. 2018). Although matched in luminosity, observations have shown that high-redshift ($z > 1$) U/LIRGs are very different from their local counterparts. Many authors have noted differences in their SEDs (e.g. Farrah et al. 2008; Muzzin et al. 2010), physical properties, and morphologies (e.g. Kartaltepe et al. 2012). High-resolution studies have revealed that the star-forming regions of high-z U/LIRGs are relatively extended with effective radii of order 3–16 kpc (e.g. Iono et al. 2009; Tacconi et al. 2013), while the extent of star formation in local U/LIRGs are much more compact with sizes of 0.3–2 kpc (e.g. Pereira-Santaella et al. 2018). Dynamically, high-redshift U/LIRGs appear to be a mixture of mergers and disc galaxies, with spatially resolved observations revealing large rotating discs at $z \sim 2$ with SFRs in the hundreds of $M_\odot\ {\rm yr}^{-1}$ without any sign of ongoing major merging (e.g. Förster Schreiber et al. 2009; Wisnioski et al. 2015). There also appears to be difference in the strength of far-infrared (FIR) fine-structure cooling lines arising from the interstellar medium (ISM). Local U/LIRGs are 'deficient' in the luminosity of these FIR metal lines, such as [C II] 158 μm and [N II] 122 and 205 μm, when compared to regular star-forming galaxies and high-z U/LIRGs (e.g. Graciá-Carpio et al. 2011; Rigopoulou et al. 2014; Díaz-Santos et al. 2017).

Intermediate-redshift U/LIRGs ($0.2 < z < 0.7$) straddle the region of high-z and local galaxies. Pereira-Santaella et al. (2019) found that intermediate-z U/LIRGs seem to be at an earlier stage of interaction and have a lower dust temperature than local U/LIRGs, but have a similar level of dust obscuration. Rigopoulou et al. (2014) and Magdis et al. (2014) showed that the SFE, dust, and [C II] emission lines in the ISM all exhibit characteristics that more closely resemble star-forming MS galaxies than local U/LIRGs. This hints at a gradual evolution in the properties U/LIRGs from high-z to low-z, where by $z \sim 1$ the equivalent of local disc galaxies are LIRGs and by $z \sim 2$ the equivalent are ULIRGs.

The latest generation near-IR spectrographs, such as the *K*-band Multi Object Spectrograph (KMOS) and Multi-Object Spectrometer For Infra-Red Exploration (MOSFIRE), have enabled large-scale kinematic studies of galaxies at high z. The KMOS^{3D} survey (Wisnioski et al. 2015), KMOS Deep Survey (Turner et al. 2017), MOSFIRE Deep Evolution Field (MOSDEF Kriek et al. 2015), KMOS Redshift One Spectroscopic Survey (KROSS Stott et al. 2016), and Survey in the near-Infrared of Galaxies with Multiple position Angles (SIGMA Simons et al. 2016) provide hundreds of galaxies up to $z \sim 4$ and spanning $10^9\ {\rm M}_\odot < M_\star < 10^{11.5}\ {\rm M}_\odot$. These show that up to 80 per cent of the high-mass end appear to be rotation dominated and have baryon to dark matter ratios greater than one within their effective radii, with this baryonic-dark matter ratio increasing with redshift (e.g. Wuyts et al. 2016; Genzel et al. 2017; Price et al. 2020). The discs appear to be thicker (e.g. Elmegreen & Elmegreen 2006) and have a larger velocity dispersion suggestive of a more turbulent ISM (e.g. Übler et al. 2019). As of yet, no kinematic studies have focused solely on the massive high-z dusty star-forming galaxies so it is unclear how $z \sim 2$ luminous IR galaxies fit into this picture. It remains to be determined whether the proportion of luminous IR galaxies that are rotation dominated matches that of the general star-forming population or whether large dusty galaxies deviate from the general population.

Observations show that the SFE and gas fraction increase with both distance above the MS and lookback time, although broadly remains constant along the MS in a given epoch and is independent of $M_\star$ (e.g. Magdis et al. 2012; Genzel et al. 2015; Scoville et al. 2017; Tacconi et al. 2018; Piotrowska et al. 2019). It also appears that MS galaxies are responsible for up to 90 per cent of the cosmic SFRD (e.g. Rodighiero et al. 2011; Sargent et al. 2012) and the density of large dust-obscured galaxies increasing with redshift (e.g. Floc'h et al. 2005). This is suggestive that a substantial fraction of high-z luminous IR galaxies should be scaled up versions of local star-forming disc galaxies with their increased SFRs due to the comparatively larger reservoirs of molecular gas at high redshift (e.g. Daddi et al. 2010a; Tacconi et al. 2013; Combes 2018).

Simulations show that since $z \sim 6$ merger-driven star formation accounts for only 25 per cent of today's stellar mass (Martin et al. 2017) and may be responsible for as little as 1 per cent of the SFRD at $z = 2$ (Rodríguez Montero et al. 2019). As U/LIRGs account for as much as 50 per cent of the SFRD at cosmic noon, they act as useful test cases for these simulations.

To fully understand the evolution of U/LIRGs and how they fit into the cosmic star formation history (SFH) it is necessary to study the underlying mechanisms driving the high SFRs in the U/LIRG population at cosmic noon. We need to investigate the properties of IR luminous galaxies and compare these properties to the general star-forming population at this epoch in order to understand U/LIRGs contribution to the SFRD and to track the evolution of U/LIRGs in the range $0 < z < 2$.

In this paper, we present integral field spectroscopy (IFS) with KMOS on the Very Large Telescope (VLT) of a sample of dusty star-forming galaxies at cosmic noon. In Section 2, we define our sample selection and how we undertook our observations. In Section 3, we show how we analysed the data to find the spectra, SFRs, and kinematics. Section 4 examines the mechanisms driving the huge SFRs of our sample and discusses their evolution across cosmic time. In Section 5, we sum up our results. When required, values of $H_0 = 70\ {\rm km\ s^{-1}\ Mpc^{-1}}$, $\Omega_{\rm m} = 0.3$, and $\Omega_\Lambda = 0.7$ were used in this paper. When required the initial mass function (IMF) was assumed to be a Chabrier (2003) form.

2 OBSERVATIONS

2.1 The sample

The galaxies studied here were drawn from Herschel observations of the Great Observatories Origins Deep Survey South field (GOODS-S, Elbaz et al. 2011). GOODS-S benefits from the availability of excellent multiwavelength ancillary data (e.g. ZFOURGE, Straatman et al. 2016) including multiple photometric bands, stellar masses etc. The present sample (hereafter our KMOS sample) comprises 18 targets which were selected according to the following criteria:

(i) Detection in at least one of the Herschel bands to ensure the U/LIRG-like infrared luminosity of the galaxies and therefore high SFR.

(ii) Spectroscopic redshift or very robust photometric redshift based on at least 10 data points from broad-band photometry.

(iii) Galaxies located in the $2 < z < 2.5$ regime – this redshift is chosen to allow the Hα spectral line (6563 Å) and the [N II] fine-structure doublet (6549 and 6583 Å) to be observed by KMOS.

(iv) All targets have Spitzer 24 μm counterparts.

(v) All targets could be simultaneously observed in one KMOS pointing.

2.2 Integral field spectroscopy

KMOS is an Integral Field Spectrograph in operation on the VLT that can simultaneously target up to 24 objects within a patrol field of 7.2 arcmin in diameter (Sharples et al. 2013). Each integral field unit (IFU) has a square field of view of 2.8 arcsec $\times$ 2.8 arcsec. This field of view is divided into 14 $\times$ 14 pixels giving a seeing limited spatial sampling of 0.2 arcsec. The typical spectral resolution within the *K* band is 4200 with a 2 channel full width at half-maximum (FWHM).

All of our 18 objects were prepared using the KMOS Arm Allocator (KARMA, Wegner & Muschielok 2008), with each galaxy assigned to an IFU allowing all targets to be observed in a single pointing, ensuring atmospheric conditions are the same across the sample. Observations were taken in the *K* band which has coverage of 1.934–2.460 μm and a resolution of approximately 3 Å.

The data are made up of 12 separate observation blocks (OBs): six on 2013 November 22/23 and six on 2016 October 9/10.[1] We used the 'stare' observation mode, with eight exposures per OB with an integration time of 600 s per exposure. One IFU was dedicated to a star so we could measure the point-spread function (PSF) for each OB. The seeing varied from 0.3 to 1.3 arcsec over the two nights and the average seeing conditions were approximately 0.6 arcsec.

The raw data were reduced using the standard KMOS pipeline, part of the EsoReflex package (Davies et al. 2013; Freudling et al. 2013). The pipeline carries out dark current correction, flat-field correction, wavelength calibration, telluric correction, sky subtraction, and flux calibration to produce a final data cube and an associated noise cube for each target in each OB. We took the reduced cube from each OB and combined them together to produce a final data cube per target, including the star used to measure the PSF. To account for spatial offsets across the OBs, we found the centre of the PSF via fitting 2D Gaussian to the star and shifted each cube so that the centres aligned for all 12 OBs. This gives our final cubes a spatial dimension of 17 $\times$ 16 pixels. We used a weighted average rather than a simple average to account for the observations being carried out under varying seeing conditions. This weighting was calculated by finding the area in arcseconds enclosed by each of the 12 PSFs and summing these together to get a total area. We then found the fractional contribution to the total area by each OB's PSF. The reciprocal of these fractions was then used to assign a weighting for each OB with the sum of all 12 weightings equalling one, i.e. an OB with worse than average seeing has a larger than average fractional contribution to the total area and is thus proportionally down-weighted and vice-versa for an OB with above average seeing. The PSF for the final stacked cubes was found by fitting a Gaussian to the stacked observation of the star, combined using the same weighted average, which gave a PSF FWHM of 0.57 $\times$ 0.44 arcsec.

[1]OB IDs: 200297829-41, 200402165-177 200402203-11

3 ANALYSIS

3.1 Spectra

To find the Hα and [N II] emission lines, we inspected the cube at the expected Hα wavelength based on the redshift of the galaxy. Once the emission lines were identified, individual apertures were applied to each data cube to distinguish between galaxy and sky emission. Two apertures were applied to each cube: the galaxy aperture and the sky aperture. The galaxy aperture was scaled to cover the extent of the galaxy emission. The remaining spaxels were dedicated to the sky aperture, which was normalized to be the same area as the galaxy aperture.

All spaxels within the galaxy apertures were collapsed into a one-dimensional spectrum and model spectra were fitted to the observed Hα and [N II] emission lines. This model involved simultaneously fitting three Gaussian profiles and a linear function to account for any continuum. The ratio of the [N II] 6583 Å/ [N II] 6549 Å peak flux was preset to 0.34 as predicted theoretically (e.g. Osterbrock & Ferland 2006) and the width of the [N II] Gaussian profiles was forced to equal the width found for the Hα emission line. All three lines were also forced to share the same line of sight velocity. The best fit was determined by a χ^2 minimization to the observed flux. For galaxy o13 the [N II] lines are not detected and their expected line centres coincide with a trough in the observed spectra, which affected the fitting of the model spectra. Instead, this was fitted with a single Gaussian curve, centred on the Hα line, and a linear function.

To ensure we did not miss any Hα flux, we created a sky spectrum by collapsing all spaxels within the sky aperture and compared the sky spectrum to the integrated galaxy spectrum. If any Hα emission was found in the sky spectrum, we increased the size of our galaxy aperture and repeated the above analysis. Finally, to calculate the signal-to-noise ratio (S/N) of our spectra we used the mean and rms derived from the sky emission.

Although the pipeline does basic sky subtraction by allocating a sky IFU to the object IFU, there were still some large residual sky emission around the edge of the reduced cubes. To ensure these pixels did not skew the background rms calculations, we clipped any pixels in the sky aperture that were greater than 3σ above or below the mean sky emission.

Hα line emission was detected in 14 of the 18 targets,and the spectra shown in Figure 1. We have marginally detected ($\sim$3σ) the [N II] 6583 Å line in four of our galaxies. The total Hα and [N II] fluxes from the galaxies were evaluated by integrating the area under their respective Gaussian curves. The total Hα flux for our KMOS sample ranges from 3.07 $\times$ 10^{-17} to 8.23 $\times$ 10^{-17} erg s^{-1} cm^{-2} and an instrument-corrected FWHM of 75–473 km s^{-1}; our results are shown in Table 2. The FWHM of 75 km s^{-1} for galaxy o2 is a lower limit as a noise spike occurred on the red wing of the Hα emission line, which was corrected for in the data reduction, leading to a loss

Table 1. Our sample of luminous IR galaxies.

Object	RA*a*	Dec.*a*	z
o1	03:32:22.57	−27:45:39.11	2.073
o2	03:32:38.11	−27:44:33.67	2.330
o3	03:32:46.31	−27:44:18.07	2.433
o4	03:32:19.05	−27:43:15.29	2.409
o5	03:32:36.89	−27:42:25.76	2.142
o6	03:32:33.29	−27:42:01.82	2.455
o7	03:32:28.51	−27:46:58.95	2.309
o8	03:32:29.17	−27:45:14.61	2.434
o9	03:32:36.18	−27:46:27.51	2.291
o10	03:32:33.84	−27:45:18.09	2.141
o11	03:32:47.54	−27:44:32.86	2.276
o12	03:32:28.40	−27:42:46.52	2.141
o13	03:32:35.12	−27:40:45.21	2.312
o14	03:32:23.77	−27:41:32.15	2.304
o15	03:32:36.09	−27:42:24.57	2.139
o16	03:32:48.53	−27:45:17.50	2.169
o17	03:32:40.39	−27:44:54.88	2.227
o18	03:32:23.88	−27:42:22.19	2.331
Star	03:32:31.87	−27:41:05.97	-

Note.
[a]J2000 reference system.

of flux on the red side of the line. Intensity maps of the observed Hα for the 14 galaxies were made by summing the intensity in all channels that span the emission line, and these are shown in Fig. 2.

For three of the four targets with undetected Hα we estimated a 3σ upper limit for the line flux. First, we fitted an aperture of 1 arcsec in radius to each cube and then used the redshift of the target to find the expected peak wavelength of the Hα emission line. We found the channel that corresponds to the peak wavelength and extracted a spectrum spanning 12 channels either side (half way between the expected H-alpha and [N II] emission lines). From this we calculated the mean and standard deviation of the spectrum. Assuming the average linewidth of our sample, 267 km s^{-1} and a peak amplitude equalling the 3σ value, we estimated an upper limit for the Hα line flux. We could not get an upper limit for galaxy o11 due to a skyline falling in a couple of the channels of the expected Hα emission.

The analysis outlined in Section 2.2 was repeated but instead of the seeing weighted averaging method we recombined the cubes using a noise weighting scheme. The spectra derived from both cubes agree well within error, therefore, the choice of weighting scheme does not have a significant impact on the analysis and the results reported here.

3.2 Star formation rates

Hα emission is a sensitive tracer of star formation within the past 10 Myr as, in the absence of AGN, it is the O-type star that provides the bulk of the requisite ionizing radiation (see Kennicutt & Evans 2012 review for details on SFR tracers). Although we cannot exclude the presence of an AGN in our sample, the Hα/[N II] 6583 Å ratio is below one for the entire sample, which is consistent with the star-forming locus of the BPT diagram at z $\sim$ 2 (Shapley et al. 2015).

However, Hα is strongly attenuated by dust so in ULIRGs this provides a lower limit for the ongoing star formation (e.g. Hopkins et al. 2001). The absorption cross-section of galactic dust strongly peaks in the UV so, assuming radiative transfer balance, the IR emission is attributable to reprocessed stellar light from underlying O-type and B-type stars. This makes L_{IR} emission a probe of the SFH within the past 100 Myr (Kennicutt & Evans 2012) and is also a tracer of the galaxy's obscured star formation.

To determine the L_{IR} from our sample of galaxies, we fit the available Herschel and Spitzer photometry (Wang et al., in preparation) by using the dust model of Draine & Li (2007) following the methodology described in Magdis et al. (2013). The L_{IR} for our sample are listed in Table 3, with the fits resulting in six of our galaxies being ULIRGs, eight are LIRGs, and four could not be determined due to poor SED fits.

Taking the L_{IR} and Hα emission we can investigate the recent SFH of our sample using the following conversion factors from Murphy et al. (2011b):

$$SFR_{H\alpha} \quad (M_{\odot}yr^{-1}) \; = \; 5.37 \times 10^{-42} \, L_{H\alpha} \quad (erg\ s^{-1}), \tag{1}$$

$$SFR_{IR} \quad (M_{\odot}yr^{-1}) \; = \; 3.88 \times 10^{-44} \, L_{IR} \quad (erg\ s^{-1}). \tag{2}$$

Although these conversion factors were calibrated using a Kroupa (2001), they yield the same results as a Chabrier IMF (e.g. Chomiuk & Povich 2011, Kennicutt & Evans 2012). The $SFR_{H\alpha}$ for our KMOS sample, uncorrected for attenuation, range from 6 to 21 $M_{\odot}$ yr^{-1} with the SFR_{IR} having values ranging from 40 to 783 $M_{\odot}$ yr^{-1} (see Tables 2 and 3).

3.3 Kinematics

To investigate the kinematics of the 14 galaxies in which Hα was detected we used GalPak^{3D} (Bouché et al. 2015) which fits a rotating disc model to the observed flux. GalPak^{3D}'s Bayesian approach is well suited to recovering kinematic parameters from marginally resolved galaxies with low S/N at increasing disc radius.

GalPak^{3D}'s model galaxy has 10 free parameters: x, y, and z centroid position, flux, half-light radius, turnover radius, position angle, inclination, maximum rotational velocity, and the one-dimensional intrinsic velocity dispersion. The emission from this model galaxy is subsequently convolved with a PSF, specified by the user, and the best fit to the observed data is found via a Bayesian Markov Chain Monte Carlo (MCMC) approach.

For our input cube we cut around the Hα emission line to ensure no contamination from the [N II] lines on either side. The PSF was set to the one calculated in Section 2.2 and the KMOS instrument was chosen so that GalPak^{3D} properly accounted for the appropriate instrumental resolution. For our galaxy model we assumed that the Hα emission follows an exponential radial flux profile, the rotation curves have an arctan functional form, and the intrinsic velocity dispersion is isotropic and spatially constant across the disc. We set the aspect ratio (vertical scale height to effective radius) to 0.2, to account for thicker discs at high redshifts (e.g. Förster Schreiber et al. 2009; Wuyts et al. 2016). The spatial and kinematic parameters, listed in the previous paragraph, were left free for the MCMC to fit.

Six of the sample converged in the MCMC to parameters consistent with a rotating disc. The spatial and kinematic parameters found by GalPak^{3D} are shown in Table 4 and the model for galaxy o3 is shown in Fig. 3. We rejected model discs that converged to unphysical values, e.g. rotational velocities approaching 1000 km s^{-1} or half light radii/flux far exceeding our emission maps. Likewise, we rejected models that only converged due to a hard boundary being adopted in GalPak^{3D}, i.e. rotational velocities of 350 km s^{-1} if the hard boundary is set to 350 km s^{-1}. We rejected discs if any individual parameter was bimodal or if the model galaxy provided a poor fit to the data upon inspection of residuals between the model and observed galaxies. Galaxy o17 was omitted from this analysis as

Table 2. Values found from the Hα emission line fitting. Values in italics are estimates based on upper limits as discussed in Section 3.1.

Object	$\lambda_{H\alpha}$[a] μm	FWHM[b] km s^{-1}	$F_{H\alpha}$[c] 10^{-17} erg s^{-1} cm^{-2}	$L_{H\alpha}$[d] 10^{42} erg s^{-1}	$SFR_{H\alpha}$[e] $M_\odot$ yr^{-1}	[N II] 6583 Å/Hα[f]
o1	*2.017*	*267*	*< 5.46*	*< 1.72*	*<9*	
o2[g]	2.185	75 ± 9	5.13 ± 0.85	2.15 ± 0.37	12 ± 2	–
o3	2.253	310 ± 34	8.23 ± 1.12	3.83 ± 0.52	21 ± 3	0.34 ± 0.09
o4	2.237	305 ± 34	7.82 ± 1.11	3.55 ± 0.51	19 ± 3	–
o5	2.062	235 ± 21	4.61 ± ± 0.55	1.58 ± 0.19	8 ± 1	–
o6	2.267	126 ± 21	5.16 ± 1.14	2.46 ± 0.54	13 ± 3	0.29 ± 0.09
o7	2.172	355 ± 4	4.39 ± 0.36	1.80 ± 0.15	10 ± 1	0.45 ± 0.16
o8	2.254	368 ± 77	6.54 ± 1.81	3.05 ± 0.85	16 ± 5	–
o9	*2.160*	*267*	*< 3.53*	*< 1.41*	*<8*	–
o10	2.062	245 ± 22	3.07 ± 0.52	1.18 ± 0.20	6 ± 1	–
o11	*2.150*		–	–	–	–
o12	2.141	132 ± 22	6.30 ± 1.43	2.15 ± 0.49	12 ± 3	–
o13	2.173	473 ± 52	6.97 ± 0.95	2.87 ± 0.39	15 ± 2	–
o14	2.168	415 ± 43	7.22 ± 0.99	2.94 ± 0.40	16 ± 2	–
o15	2.060	145 ± 13	4.97 ± 0.57	1.69 ± 0.19	9 ± 1	–
o16	2.079	176 ± 17	3.67 ± 0.46	1.29 ± 0.16	7 ± 1	0.28 ± 0.09
o17	2.227	386 ± 39	7.83 ± 1.00	2.94 ± 0.38	16 ± 2	–
o18	*2.186*	*267*	*< 1.53*	*< 0.62*	*< 3*	–

Notes.
[a]Observed peak wavelength of the Hα emission line. Errors not included as they were of the order of Å and the values quoted here are in μm.
[b]The FWHM of the galaxy emission line, corrected for the instrumental FWHM.
[c]Total Hα flux of the galaxy.
[d]The total Hα luminosity of the galaxy.
[e]The SFR of the galaxy, uncorrected for dust attenuation, calculated from the Hα luminosity. See Section 3.2.
[f]The ratio of Hα flux to the flux of the [N II] 6583 Å emission line.
[g]The FWHM for o2 is a lower bound due to a noise spike on the red wing of the Hα emission line, which was corrected during data reduction.

some noisy channels in the blue wing of the emission line appeared to be affecting the best-fitting parameters.

To test our results sensitivity to the assumed galaxy model, we repeated the analysis with a Gaussian radial flux profile and subsequently rerun the analysis using GalPak^{3D}'s default aspect ratio of 0.15 and all results agreed within error.

4 THE PROPERTIES OF Z ∼ 2 DUSTY LUMINOUS IR GALAXIES

4.1 Modes of star formation

The location of a galaxy in the $M_\star$-SFR plane is strongly linked to its mode of star formation. Although neither the mass nor the SFR relies on knowledge of what the gas is doing, the SFR is implicitly modulated by gas fraction and the SFE within the galaxy (e.g. Tacconi et al. 2018). This, in turn, allows the underlying mechanism driving star formation to be inferred by a galaxy's position with respect to the main sequence. To place our sample on the MS (Fig. 4), we use the SFR_{IR} derived from the L_{IR} and the stellar mass derived from fitting Bruzual & Charlot (2003) models to the BVizYJH photometry and the Infrared Array Camera (IRAC) 3.6, 4.5, 5.8, and 8.0 μm photometric bands.

In summary, for each galaxy SED we generated a set of models using the stellar population synthesis templates of Bruzual & Charlot (2003). We adopted the Padova stellar evolution tracks (Bertelli et al. 1994) and constructed models with solar metallicity and a Chabrier IMF. We used the Calzetti et al. (2000) starburst attenuation law to account for the extinction. For the parametrization of the SFH of each galaxy we considered two simple single-component models: an exponentially declining model of the form SFR(t) ∼ exp (-t/τ) with e-folding times of τ = 0.05, 0.1, 0.5, 2.0, and 5.0 Gyr, and continuous star formation (CSF) models. Finally, we used a χ^2 minimization technique to find the best-fitting model to each galaxy SED.

We can quantify how far each galaxy lies from the MS via

$$\log(SFR_{\rm MS}) = a + b\log\left(\frac{M_\star}{M_\odot}\right) + c\log\left(\frac{M_\star}{M_\odot}\right)^2, \quad (3)$$

where $M_\star$ is the stellar mass and a = −19.99, b = 3.44, and c = −0.13 (taken from Whitaker et al. 2014). The SFR_{IR} confirm all but two of our sample to be MS as seen in Fig. 2 , with the two outliers being galaxy o7, having a distance above the MS (ΔSFR) of 0.99 dex, and o15, with ΔSFR = 0.78 dex. This suggests that star formation in luminous IR galaxies at cosmic noon is dominated by steady-state processes.

To determine τ_{dep} and thus further explore the mode of star formation in our sample of galaxies, we searched for ancillary CO or Rayleigh Jeans continuum data that would enable us to compute gas masses. Two of our KMOS sample had the requisite observations: galaxies o3 and o7. Galaxy o3 was previously studied in Wiklind et al. (2019) in which they used the same continuum method to estimate a molecular gas mass of 8.57 × 10^{10} $M_\odot$. Using this value gives a depletion time of 0.35 Gyr which is approaching that of an MS star-forming galaxy at cosmic noon (e.g. Tacconi et al. 2020).

Galaxy o7 is an interesting case as it clearly falls within the starburst regime, with its SFR of 783 ± 5 $M_\odot$ yr^{-1} It has been previously studied by Elbaz et al. (2018) and Buat et al. (2019) where,

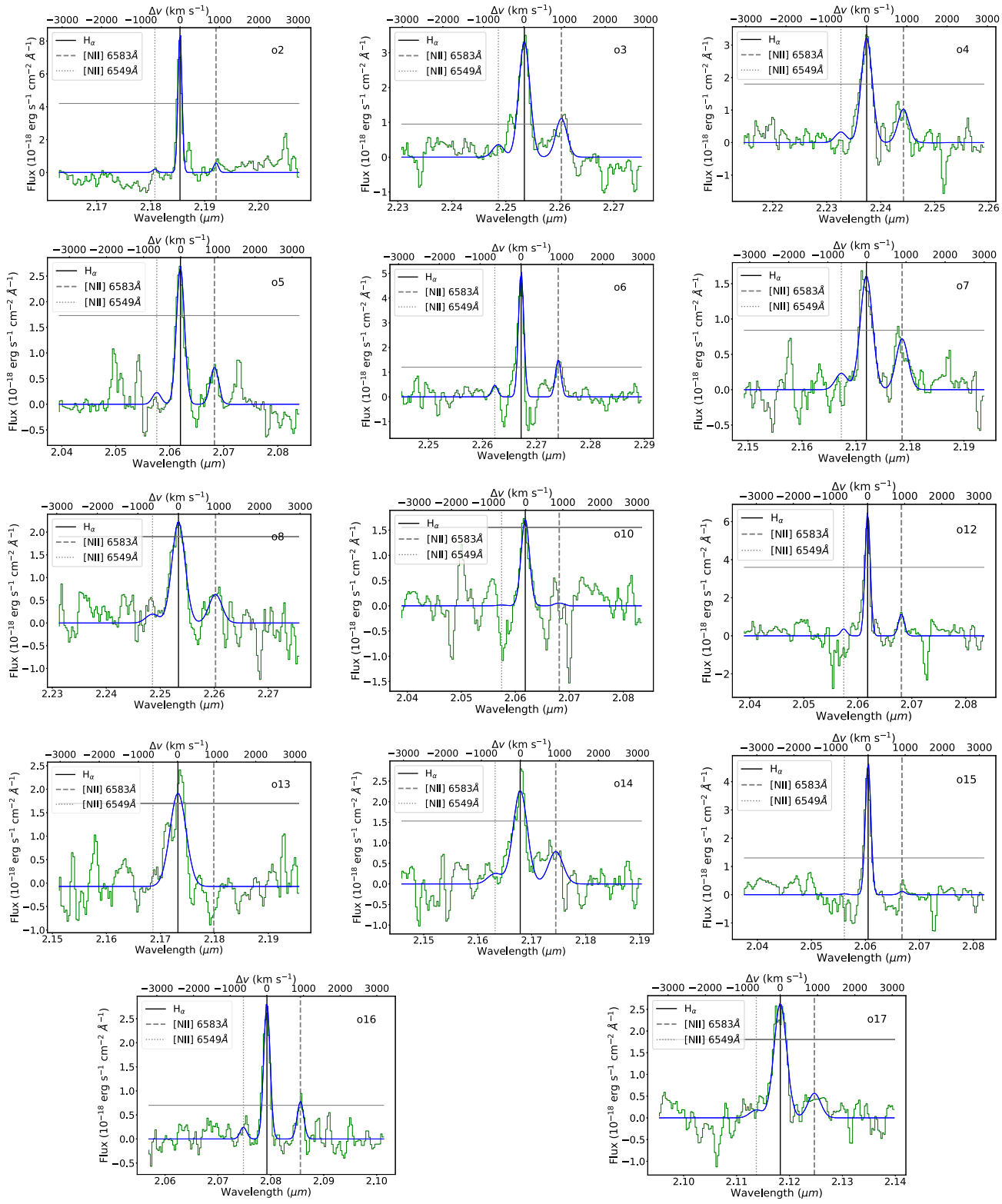

Figure 1. The integrated spectra for the 14 luminous IR galaxies with detected Hα emission. The best-fitting model, described in Section 3.1, is overlayed in blue and the vertical lines represent the peak of the red-shifted Hα and [N II] 6549 Å 6583 Å lines. The grey horizontal line indicates where the S/N equals 3.

using slightly different SED fitting methods, they found SFRs (for a Chabrier IMF) of 670 ± 34 and 567 ± 28 $M_\odot$ yr^{-1}, respectively. The galaxy has a 1.1mm continuum measurement by Franco et al. (2018) and using the Scoville et al. (2016) technique we compute a depletion time of 0.23 ± 0.2 Gyr, in line with what we would expect from a starburst. This method calculates molecular gas mass from a single point on the Rayleigh Jeans slope of the dust continuum and then converts to a molecular gas mass using assumptions such as

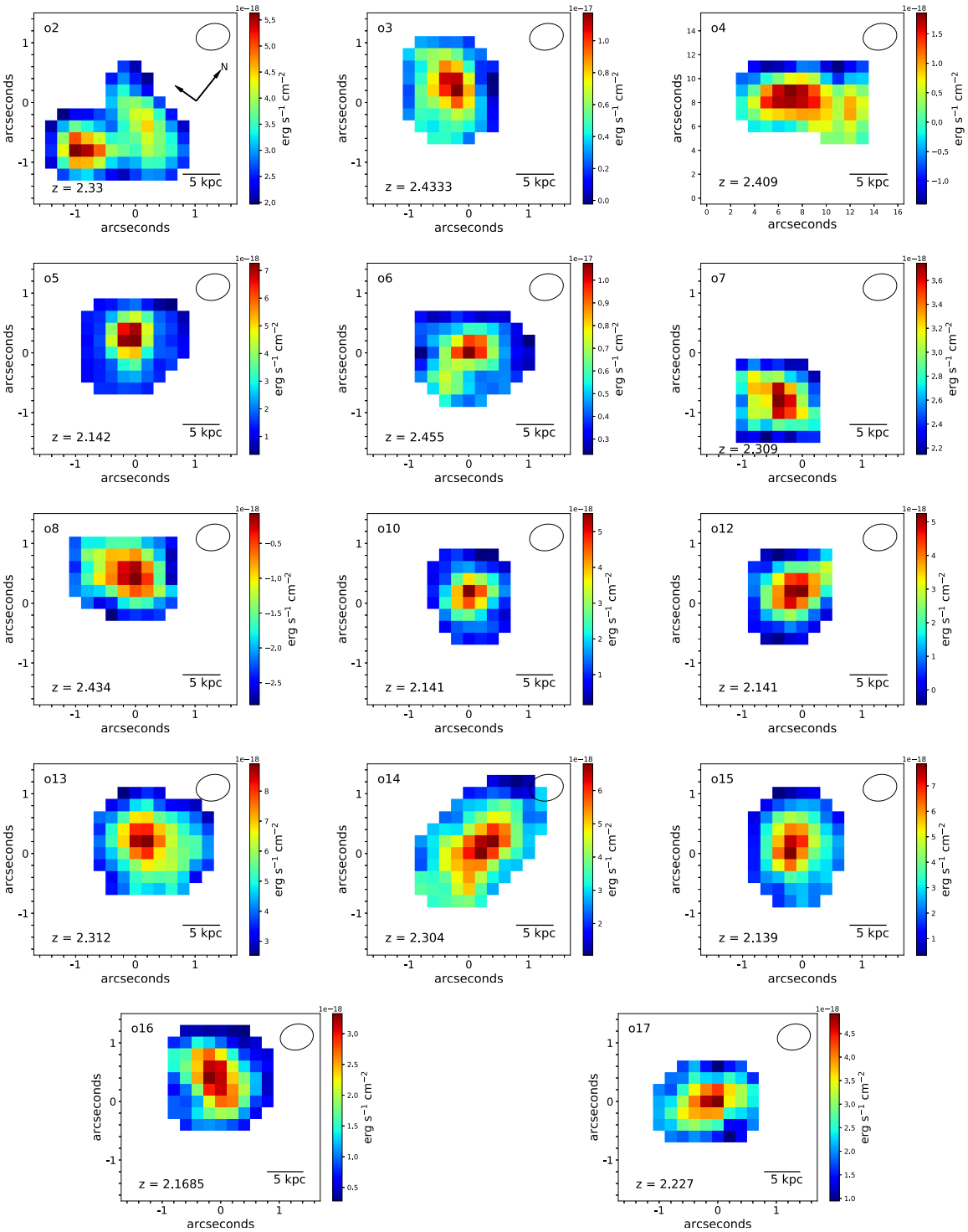

Figure 2. The emission maps of the Hα emission line (6563 Å) from our galaxy sample. Each pixel is 0.2 arcsec × 0.2 arcsec where 1 arcsec corresponds to ∼8 kpc at these redshifts. The seeing is 0.57 arcsec × 0.44 arcsec, corresponding to a resolution of ∼4 kpc, and the size of the PSF is shown in the top right corner. North and east are located 37 deg clockwise from the x-axis as shown by the arrows in the emission map of galaxy o2.

optically thin emission and conversion factors based on local galaxies. Although differing ISM conditions at high-z galaxies compared to local ones introduce uncertainty in this method, similar potential sources of error exist in the standard CO to H_2 method of finding molecular gas reservoirs in high-z ULIRGs (e.g. Bolatto, Wolfire & Leroy 2013).

The molecular gas masses and corresponding depletion times for these two galaxies agree well with our finding of one galaxy being a starburst and the other an MS based on their location on the $M_\star$-SFR plane. Recent studies (e.g. Elbaz et al. 2018; Franco et al. 2020; Valentino et al. 2020) have shown that position on the $M_\star$-SFR plane may not hold in all cases when categorizing a galaxy's mode of star

Table 3. Values found by fitting an SED to the Spitzer and Herschel photometry using the dust model of Draine & Li (2007). Values in italics are estimates based on upper limits as discussed in Section 3.1.

Object	log($M_\star$)[a] $M_\odot$	log(L_{IR})[b] erg s^{-1}	SFR_{IR}[c] $M_\odot yr^{-1}$	log($\frac{SFR_{H\alpha}}{SFR_{IR}}$)[d]	ΔSFR[e]	Dust temperature[f] K
o1	10.78	12.07 ± 0.02	176 ± 8	*< −1.28 ± 0.02*	0.26 ± 0.02	32 ± 4
o2	10.52	–	–	–	–	–
o3	10.87	12.27 ± 0.01	276 ± 6	−1.13 ± 0.06	0.40 ± 0.01	39 ± 2
o4	10.93	12.20 ± 0.01	239 ± 6	−1.10 ± 0.06	0.30 ± 0.01	34 ± 4
o5	10.39	11.48 ± 0.03	45 ± 3	−0.73 ± 0.06	−0.06 ± 0.03	–
o6	10.55	11.62 ± 0.04	62 ± 5	−0.67 ± 0.10	−0.04 ± 0.04	–
o7	10.65	12.72 ± 0.01	783 ± 5	−1.91 ± 0.04	0.99 ± 0.01	42 ± 2
o8	10.16	–	–	–	–	–
o9	10.72	11.86 ± 0.02	107 ± 5	*< −1.15 ± 0.02*	0.08 ± 0.02	–
o10	10.73	11.84 ± 0.02	102 ± 4	−1.26 ± 0.08	0.05 ± 0.02	50 ± 2
o11	10.41	11.69 ± 0.03	72 ± 4	–	0.13 ± 0.03	–
o12	10.64	11.67 ± 0.02	70 ± 3	−0.78 ± 0.02	−0.05 ± 0.02	–
o13	10.39	–	–	–	–	–
o14	10.79	12.15 ± 0.02	211 ± 9	−1.13 ± 0.06	0.33 ± 0.02	23 ± 1
o15	10.27	12.24 ± 0.01	257 ± 4	−1.45 ± 0.05	0.78 ± 0.01	34 ± 23
o16	10.41	11.43 ± 0.07	40 ± 7	−0.76 ± 0.09	−0.13 ± 0.07	–
o17	10.55	11.74 ± 0.04	82 ± 3	−0.71 ± 0.07	0.08 ± 0.04	–
o18	10.72	–	–	–	–	–

Notes.
[a]Stellar mass of the galaxy using the method described in Section 4.1. We assume an error of 15% in any calculation that required the stellar mass.
[b]IR luminosity of our sample calculated by fitting an SED using the model of Draine & Li (2007).
[c]SFR calculated from the IR luminosity. See Section 3.2.
[d]An estimate of the dust attenuation within the galaxy. See Section 4.2.
[e]The difference, in dex, between the observed SFR and the expected SFR from Whitaker et al. (2014), at the galaxy's redshift. Main-sequence galaxies lie within 0.3 dex of this expected SFR.
[f]The temperature of the dust within our galaxy estimated by fitting a modified blackbody to the FIR photometry. See Section 4.3.

Table 4. Kinematic parameters of the best-fitting model galaxy from GalPak[3D] for our sample of luminous IR galaxies.

Object	R_E[a] kpc	i[b] deg	PA[c] deg	v_{max}[d] km s^{-1}	σ_0[e] km s^{-1}	$\sigma_0(z=0)$[f] km s^{-1}	f_{gas}[g]	$v_{rot}/\sigma_0(z=0)$[h]	log(M_{dyn})[i] $M_\odot$	M_{bar}/M_{dyn}[j]
o3	3.69 ± 0.13	79 ± 4	234 ± 3	306 ± 43	148 ± 6	73 ± 18	0.62	4.2 ± 1.2	11.16 ± 0.02	0.67 ± 0.16
o5	2.33 ± 0.12	21 ± 6	1 ± 11 1	308 ± 43	103 ± 6	54 ± 13	0.47	5.7 ± 1.6	10.59 ± 0.03	0.59 ± 0.16
o8	4.01 ± 0.39	59 ± 6	88 ± 5	218 ± 48	75 ± 12	37 ± 9	0.60	5.9 ± 1.9	10.70 ± 0.06	0.36 ± 0.20
o14	6.85 ± 0.43	66 ± 3	0 ± 3	331 ± 19	138 ± 7	70 ± 17	0.61	4.8 ± 1.2	11.35 ± 0.03	0.35 ± 0.16
o15	3.16 ± 0.10	25 ± 3	157 ± 4	314 ± 45	46 ± 4	24 ± 6	0.87	13.0 ± 3.7	10.37 ± 0.02	2.99 ± 0.16
o16	5.01 ± 0.18	61 ± 3	62 ± 2	75 ± 16	97 ± 0	50 ± 12	0.42	1.5 ± 0.5	10.75 ± 0.04	0.40 ± 0.18

Notes.
[a]Half-light radius of Hα emission assuming an exponential Sersic profile.
[b]Galaxy inclination.
[c]Position angle east of north to the blue-shifted major kinematic axis.
[d]De-projected maximum velocity of the asymptotically flat part of the rotation curve.
[e]Intrinsic velocity dispersion of galaxy disc.
[f]The expected velocity dispersion of the galaxy at $z = 0$ assuming the redshift evolution of velocity dispersion. See Section 4.4.
[g]Estimated gas fraction of the galaxy. See Section 4.5.
[h]The dynamical ratio of the galaxy assuming the corrected velocity dispersion at $z = 0$.
[i]Dynamical mass of the galaxy. See Section 4.5.
[j]Fraction of the total galaxy mass comprised of baryonic matter. See Section 9.

formation, with some massive $z \sim 2$ MS galaxies exhibiting high SFEs and very short depletion time-scales. Such objects appear to have compact star formation and are gas poor compared to their MS counterparts and it is suggested (e.g. Dekel & Burkert 2014; Popping et al. 2017) that these galaxies are at the end of their starburst phase and are the progenitors of massive elliptical galaxies. Conversely, case studies of starbursting submillimetre galaxies (SMGs) have signatures consistent with rotating discs (e.g. Hodge et al. 2019; Drew et al. 2020), so distance above the main sequence does not always imply a merger.

Our analysis indicates that the majority of our sample of galaxies are consistent with being secularly evolving MS galaxies with only o7 and o15 being starbursts. Future observations of the molecular gas content of these galaxies likely confirm this finding.

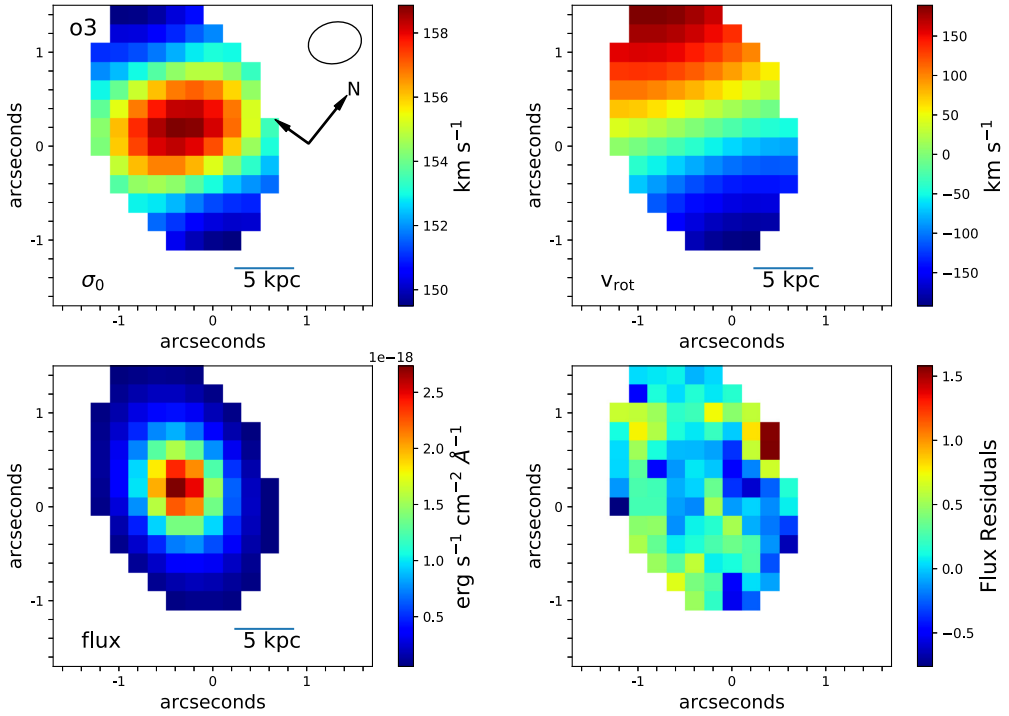

Figure 3. Maps of the model galaxy from GalPak^{3D}, for galaxy o3, convolved with the PSF of 0.57 arcsec × 0.44 arcsec, but excluding background/sky. The top left panel shows the intrinsic velocity dispersion across the galaxy disc. The top right panel shows the projected velocity field assuming the systematic velocity of the galaxy has been set to zero. The bottom left panel shows the flux arising from the model disc which is assumed to have an exponential Sersic brightness profile. The bottom right panel shows the residuals of the best-fitting flux when compared to the observed cube. North and east are located 37 deg clockwise from the x-axis as shown by the arrows in the top left panel.

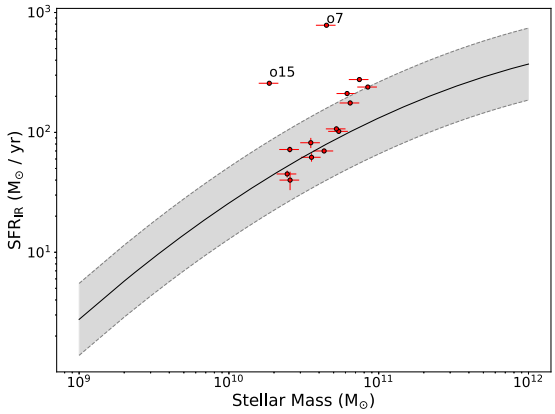

Figure 4. The SFR$_{IR}$ from our sample of luminous IR galaxies plotted against the M$_\star$, with the main sequence of Whitaker et al. (2014) represented by the grey shaded region. The solid line is the main sequence at z = 2.25 and the grey region represents 0.3 dex above and below this relation. Galaxies o7 and o15 fall within the starburst regime.

4.2 Obscured versus unobscured star formation

As our luminous IR galaxies emit strongly at FIR wavelengths >100 μm a priori we know these to be dusty star-forming galaxies. Hα is strongly attenuated by dust so it is likely to underestimate the true SFR. In compact star-forming galaxies, e.g. mergers, the SFR$_{H\alpha}$ can be orders of magnitude lower than IR estimates of SFR (e.g. Rodríguez-Zaurín et al. 2011). High-redshift U/LIRGs have more extended star formation with lower SFR surface densities so for a given IR luminosity attenuation is expected to be weaker at high-z (e.g. Buat et al. 2015).

As mentioned in Section 3.2, Hα and FIR emission arises from stellar populations with different age ranges, 10 and 100 Myr, respectively. If we assume a constant SFH in the past 100 Myr, we can take the ratio of log(SFR$_{H\alpha}$/SFR$_{IR}$) as a proxy for the obscured versus unobscured star formation. This allows us to investigate how dust enshrouded our sample is when compared to intermediate-z U/LIRGs in Pereira-Santaella et al. (2019) and local U/LIRGs from Rodríguez-Zaurín et al. (2011).

The average log(SFR$_{H\alpha}$/ SFR$_{IR}$) ratio of our sample is -1.08 ± 0.34 (or -1.06 ± 0.37 when excluding the Hα upper bounds), while the value for the intermediate-z U/LIRGs is -2.2 ± 0.4, with values of -2.0 ± 0.5 and -1.6 ± 0.5 for the local ULIRGs and LIRGs, respectively. Our sample has similar log(SFR$_{H\alpha}$/ SFR$_{IR}$) to local LIRGs (see Fig. 5) with only galaxy o7, a starburst, falling within the location of local ULIRGs. This demonstrates that for the same L$_{IR}$, high-z U/LIRGs appear to be less dust obscured than their local and intermediate-redshift counterparts.

Despite our sample size being relatively small there is a statistically significant correlation between the magnitude of obscuration and a galaxy's distance from the MS, as shown in Fig. 6, with a linear fit giving a Pearson's $\rho = -0.88$ and a P-value <0.001. Follow-up continuum studies of the dust distribution within our sample of galaxies are needed to further investigate this correlation.

4.3 Dust temperature

Dust properties within a galaxy can be inferred from the Rayleigh Jeans regime of the FIR emission (e.g. Casey, Narayanan & Cooray

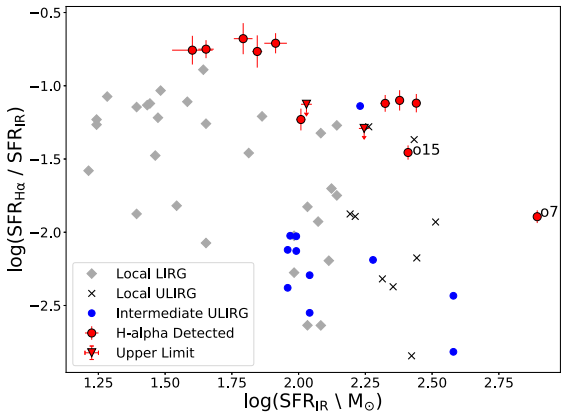

Figure 5. The log ratio of SFR$_{H\alpha}$/SFR$_{IR}$ versus log(SFR$_{IR}$) which is used as a proxy for dust obscuration. Our sample (red) is compared to samples of intermediate-z and local U/LIRGS from Pereira-Santaella et al. (2019) and Rodríguez-Zaurín et al. (2011), respectively. The average log ratio of our sample is -1.2 ± 0.4, while the log ratio for the intermediate-z U/LIRGs, local ULIRGs, and LIRGs is -2.2 ± 0.4, -2.0 ± 0.5, and -1.6 ± 0.5, respectively. Galaxy o7 and o15 are marked as both of these galaxies fall above the main sequence, with o7 being the only one of our sample to fall within the range of the local ULIRGs.

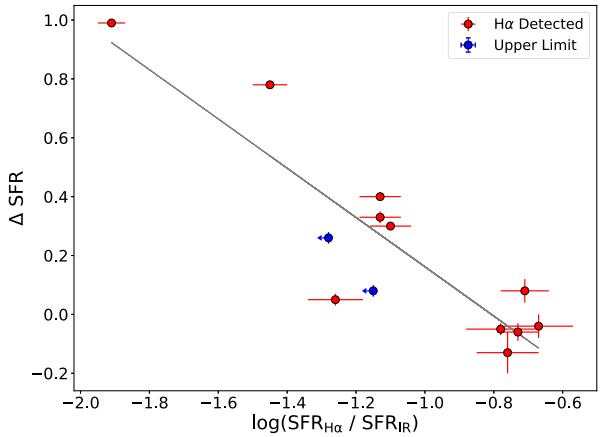

Figure 6. The relation between extinction, as represented by log(SFR$_{H\alpha}$/SFR$_{IR}$), and a galaxies vertical offset from from the main sequence of Whitaker et al. (2014), in dex, represented by ΔSFR. The linear fit has a Pearson's $\rho = -0.88$ and shows that the level of obscured star formation increases with distance above the main sequence.

2014). A single modified blackbody fitted to the FIR photometry is sufficient to determine the cold temperature of large dust grains, whereas a mixture of modified blackbodies is required to account for the warm dust of the smaller dust grains (e.g. Draine & Li 2007).

Using our Herschel photometry, and limiting ourselves to wavelengths >100 μm to ensure we are sampling the peak and Rayleigh Jeans slope of the emission, we fit a modified blackbody to evaluate the cold dust temperature (T$_{dust}$) for our sample. We assumed a grey-body emission model of the form:

$$F_\nu[(\nu_{obs}, T_d/(1+z), \beta] = (1 - e^{-\tau})B_\nu(\nu_{obs}, T_d/(1+z)), \quad (4)$$

with

$$\tau = \left(\frac{\nu}{\nu_0}\right)^\beta,$$

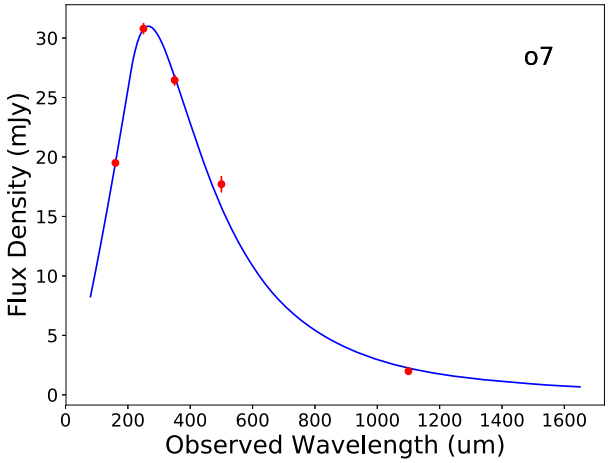

Figure 7. The modified blackbody, as described in Section 4.3, fitted to the photometry of galaxy o7. The best fit from the MCMC is plotted in blue and the observed flux is given by the red data points.

where F$_\nu$ is the flux density in Jy, β is the emissivity coefficient, ν_0 is the rest-frame frequency at which the optical depth reaches unity, and B$_\nu$(ν_{obs},T$_d$) is the blackbody function. Due to the small number of photometry points we adopted the Markov chain Monte Carlo (MCMC) approach of Dowell et al. (2013) to fit the FIR emission. This MCMC model uses a power law for the Wien side of the peak, $F_\nu \propto \nu^{-\alpha}$, giving the model five free parameters in total: α, β, T_{dust}, ν_0, and a normalization factor (see Dowell et al. 2013 for full details). We assumed that the dust emission is optically thin, has a single dust temperature rather than a multidust temperature model, and the emissivity parameter was set to $\beta = 1.5$ (e.g. Casey et al. 2014). We fit a grey-body to galaxies with three or more photometry points >100 μm and relaxed the Wien power law condition, reverting to a standard grey-body, for those galaxies that had only three photometric data points available. Seven of our KMOS sample had the requisite photometry data and we compute a range of temperatures between 23 and 50 K, with an average value of 36 ± 8 K (see Table 3 and Fig. 7).

Previous studies have found that the intensity of the radiation field increases with lookback time (e.g. Magdis et al. 2012; Huang et al. 2014; Béthermin et al. 2015) along with a concurrent rise in dust temperatures, within MS galaxies, back to z $\sim$ 2 (e.g. Magnelli et al. 2014). Local U/LIRGs have $T_d \sim$ 30–55 K (e.g. Clements et al. 2018), while local normal star-forming galaxies detected by the Herschel Space Observatory have colder dust with an average $T_d \sim$ 20 K (Cortese et al. 2014). Dust temperatures for z $\sim$ 2 ULIRGs have been found in the range 25–60 K (e.g. Magdis et al. 2010; Symeonidis & Page 2018), providing evidence that ULIRGs do not follow the same redshift-T$_d$ trend as MS galaxies.

On the other hand, z $\sim$ 2 galaxies lying above the MS often contain warmer dust than what is found in local ULIRGs, e.g. Miettinen et al. (2017) find T_d values up to 79 K. High-z star-forming galaxies hosting an AGN can have a similar range of dust temperatures as their non-AGN counterparts (e.g. Chen et al. 2021), but extremely luminous AGN such as dust-obscured quasars tend to have higher temperatures, with studies showing an average T$_d$ > 60 K (e.g. Fan et al. 2017; D'Amato et al. 2020).

Comparing our dust temperatures to previous results, and noting we have no evidence of an AGN within our sample, we reaffirm our findings, in Section 4.1, that the T$_d$ is consistent with MS star-forming

galaxies and the SFR appear to be driven by secular steady-state processes.

4.4 Dynamical ratio

The dynamical ratio is defined as the ratio between the rotational velocity, v_{rot}, and the velocity dispersion, σ_0, of a galaxy. The mean observed velocity dispersion increases as galaxies go from isolated, to interacting, and finally merging with a subsequent decrease in the amplitude of the rotational velocity (e.g. Bellocchi et al. 2013). Hence, high dynamical ratios correspond to isolated discs with lower ratios signifying mergers and interactions.

Pereira-Santaella et al. (2019) used the dynamical ratio to categorize intermediate-z U/LIRGs into isolated or interacting/merging galaxies by comparing their kinematics to the v_{rot} and σ_0 observed in an isolated sample and an interacting sample of local U/LIRGs. Threshold values of $\sigma_0 < 56$ km s^{-1} and $v_{rot}/\sigma_0 > 3.2$ separate the isolated subgroup from the interacting subgroup of local U/LIRGs (for full details see Pereira-Santaella et al. 2019).

To apply this method to our sample, we first need to account for the star-forming ISM at high-z being more turbulent due to an increased molecular gas fraction (e.g. Bauermeister et al. 2013; Saintonge et al. 2013; Übler et al. 2019). Therefore, a $\sigma_0 > 56$ km s^{-1} at high-z can be driven purely by internal dynamic processes and a more turbulent ISM does not always imply a recent merger or interaction. We use the redshift evolution of the intrinsic velocity dispersion to account for this increase in σ_0 as a function of redshift, allowing the thresholds values ascertained in local U/LIRGs to classify our sample. We take the following relation from Übler et al. (2019), which holds for ionized gas:

$$\sigma_{0,\mathrm{fit}}(z)/kms^{-1} = (23.3 \pm 4.9) + (9.8 \pm 3.5) \times z. \quad (5)$$

By plugging the redshifts of our luminous IR galaxies into this equation, we can find the expected intrinsic velocity dispersion for each galaxy. We then take the ratio of this with the velocity dispersion at z = 0 to find a correction factor ($\sigma_{0,\mathrm{fit}}(z = U/LIRG)$ / $\sigma_{0,\mathrm{fit}}(z = 0)$) which gives us the expected fractional increase in σ_0 between z = 0 and the redshifts of our galaxies. We then rescale the σ_0 found by GalPak^{3D} by this correction factor to get our redshift-corrected velocity dispersion. E.g. for galaxy o3 the expected $\sigma_{0,\mathrm{fit}}(z = 2.433)$ is 46.6 km s^{-1} which is 2.03 times higher than $\sigma_{0,\mathrm{fit}}(z = 0)$, rescaling the observed $\sigma_0 = 148$ km s^{-1} to the redshift-corrected $\sigma_0 = 73$ km s^{-1}.

To increase the size of our KMOS sample, we supplemented it with targets from the ESO archive (hereafter known as the supplemental sample) which satisfied our criteria, outlined in Section 2.1, with the addition that all archival targets are also in the ZFOURGE database to ensure the supplemental sample occupied the same region of the SFR-$M_\star$ parameter space as our KMOS sample. 28 galaxies (see Table A1 in the Appendix) from the archive satisfied our criteria, with two of these flagged as AGN in ZFOURGE, and the Gaussian FWHM of their PSFs ranged from 0.5 to 0.94 arcsec. The archival galaxies were reduced and modelled following the same procedure as our KMOS sample (see Section 3.3). We note that we have identified a separate observation of our galaxy o17 in the archive (GS4 35056 in Table A1). The reduced cube from this observation did not have the issue of the noisy sky on the blue wing channels of the Hα line that was identified in our analysis (see Section 3.3), so we decided to include the archival GS4 35056 cube in the supplemental sample. This cube is used for the kinematic analysis only and to avoid confusion we will continue to refer to it as part of the supplemental sample. 12 of the supplemental sample converged with neither of the two AGNs found to be a disc (see Table A2).

From the entire sample (ours and the ESO supplemental) 15/41 appear to be isolated discs and this fraction increases to 17/41 if we use just the criterion of $v_{rot}/\sigma_0 > 3.2$ for the undetermined cases (see Figure 8). The majority of galaxies that converged in GalPak^{3D} are isolated discs and this is an artefact of fitting a model galaxies to z $\sim$ 2 observations. The KMOS spectral resolution at 2 < z < 2.5 is $\sim$40 km s^{-1} so galaxies with dynamical ratios below unity, i.e. low v_{rot}, may not have the requisite data points to constrain the turnover radius and rotational velocity of a fitted model galaxy. Likewise, galaxies with disturbed morphology (e.g. galaxy o2 in Fig. 2) can either prevent the model parameters converging or converge to a poor fit as GalPak^{3D} assumes a smooth rotating model disc. Factoring in the drop in S/N at increasing radii, GalPak^{3D} will be biased towards isolated discs with large rotational velocities at z $\sim$ 2. Therefore, a proportion of the 22 galaxies in which GalPak^{3D} could not fit a model are likely to be interacting discs, although we cannot quantify this using the above analysis.

Our findings agree with previous result of interacting versus isolated discs at this redshift. Kartaltepe et al. (2012) using *HST* imagery concluded that $\sim$50 per cent of galaxies appear to have some form of interaction and Molina et al. (2017) found 3/5 of Hα selected MS galaxies from z = <2.23> have signatures of merging based on kinemetry, a method quantifying the asymmetry in the v_{rot} and σ_0 maps allowing galaxies to be classified into ordered rotation or disturbed kinematics (Krajnović et al. 2006).

The KMOS^{3D} survey (Wisnioski et al. 2019) finds 49–70 per cent of MS galaxies ($10.00 < \log(M_\star/M_\odot) < 11.75$) at z $\sim$ 2 to be discs. The range corresponds to the exact criteria used for the classification (see Wisnioski et al. 2019 for a detailed description of their criteria). When all five of their criteria are satisfied then the fraction of disc galaxies found is 49 per cent with the value increasing to 70 per cent when considering only the first two criteria. At lower redshifts, the KROSS survey found 83 per cent of star-forming galaxies at z $\sim$ 0.9 to be rotation dominated (using the definition of $v_{rot}/\sigma_0 > 1$; Johnson et al. 2018). Using the same definition, Turner et al. 2017 found that 34 ± 8 per cent of typical star-forming galaxies at z $\sim$ 3.5 are rotation dominated.

Differences in methodology and classification has been investigated by Rodrigues et al. (2017) where they find a smaller fraction of discs than Wisnioski et al. (2015), from the same KMOS^{3D} sample of 41 galaxies at z $\sim$1, by using a different methodology to derive the kinematic parameters, such as the σ-peak or the kinematic centre, and applying the five KMOS^{3D} survey criteria described above. Rodrigues et al. (2017) also showed that some observations were misclassified as discs when broad-band images were investigated. Where possible we have verified the position angle and inclination, via the *Hubble Space Telescope* ACS/WFC camera (see Fig. C1). Where adequate S/N was available to fit isophotes to the broad-band observations, the position angle for both our KMOS and supplemental samples agrees to within 30° and the inclination to within 24°, and corroborate our fraction of isolated discs.

It is instructive to look at how the properties of the z$\sim$2 KMOS sample compares with similar luminosity samples at lower redshifts. Pereira-Santaella et al. (2019) found 10–25 per cent of their intermediate-z sample to be isolated discs, while this fraction goes down to $\sim$5 per cent for local U/LIRGs with $\log(L_{IR}/L_\odot) > 11.6$ (Bellocchi et al. 2013). Despite differences in sample sizes and systematic errors, the dynamical ratios suggest that the percentage of mergers and interactions in luminous IR systems decreases with lookback time.

The results presented here also agree with the evolution predicted by cosmological simulations. The Horizon-AGN hydrodynamical

simulation (Martin et al. 2017) shows that mergers only account for 25 per cent of stellar mass since z ≈ 6 meaning smooth accretion is the dominant driver of star formation through cosmic time. Rodríguez Montero et al. (2019), using the SIMBA simulation, find that mergers contribute only about ∼1 per cent of to the SFR density at z ∼ 2, although they does not include the pre-merger phase in their merging sample.

4.5 Dynamical mass

We can infer dynamical masses and dark matter fractions for our sample from the best-fitting kinematics. Using the methodology of Price et al. (2016) the dynamical mass can be calculated from

$$M_{\rm dyn}(R_{\rm E}) = k_{\rm eff}(R_{\rm E})\frac{V_{rms}(R_{\rm E})^2 R_{\rm E}}{G}, \quad (6)$$

where G is the gravitational constant, $k_{\rm eff}(R_{\rm E})$ is the effective virial coefficient, $R_{\rm E}$ is the half light radius, and $V_c(R_{\rm E})$ is the root mean square velocity, defined as

$$V_{\rm rms}(r) = \sqrt{V_{\rm rot}(r)^2 + \sigma_0^2}. \quad (7)$$

The effective virial coefficient is given by

$$k_{\rm eff}(R_{\rm E}) = \frac{k_{\rm disp} + k_{\rm rot}(V_{\rm rot}(R_{\rm E})/\sigma_0)^2}{1 + (V_{\rm rot}(R_{\rm E})/\sigma_0)^2}. \quad (8)$$

We chose $k_{\rm disp} = 5$ (e.g. Pettini et al. 2001) and set $k_{\rm rot} = 1$, (e.g. Miller et al. 2011), which are valid for a spherical potential. The effective virial coefficient term accounts for the existence of a non-negligible pressure component due to the more turbulent ISM at high-z (e.g. Förster Schreiber et al. 2009; Wuyts et al. 2016), and when $V_{\rm rot}(R_{\rm E})/\sigma_0 \gg 1$ equation (6) reverts to the dynamical mass calculated from only rotational support .[2]

In the absence of molecular gas observations for most of the galaxies in our sample, we estimate the gas fraction from the following:

$$f_{\rm gas} = \frac{M_{\rm gas}}{M_\star + M_{\rm gas}} = \frac{1}{\frac{M_\star}{SFR}\frac{SFR}{M_{\rm gas}} + 1} = \frac{1}{1 + (\tau_{\rm dep} \cdot sSFR)^{-1}}. \quad (9)$$

We approximate $\tau_{\rm dep}$ by using the redshift evolution of depletion time from Wisnioski et al. (2015):

$$\tau_{\rm dep}[\rm Gyr] = 1.5 \times (1+z)^{\alpha}, \quad (10)$$

We assume an α value of -1 to match that of Wisnioski et al. (2015) and Tacconi et al. (2013) and choose a pre-factor of 1.5 Gyr to represent the typical depletion time of a z = 0 MS galaxy (e.g. Saintonge et al. 2013). Rearranging equation (9) and using the fitted $M_\star$ and $SFR_{\rm IR}$ for our KMOS sample and the $M_\star$ and $SFR_{\rm IR}$ from ZFOURGE for the supplementary sample (see Table A1, and Straatman et al. 2016 for methodology), we deduce both a value for the $M_{\rm gas}$ and a value for the total baryonic mass, $M_{\rm bar} = M_{\rm gas} + M_\star$. We did not calculate a baryonic mass for galaxy o8 as we do not have a fitted $SFR_{\rm IR}$ from which to estimate the gas fraction.

By taking the ratio of baryonic mass to the dynamical mass we can subsequently get the dark matter fraction within one $R_{\rm E}$:

$$f_{\rm D} = 1 - \frac{M_{\rm bar}(R_{\rm E})}{M_{\rm dyn}(R_{\rm E})}. \quad (11)$$

To calculate the baryonic mass within one effective radii, we assume that half of the stellar mass is within one $R_{\rm E}$ and a constant gas to stellar mass ratio throughout the disc, i.e. half the gas mass is also inside one $R_{\rm E}$. This is valid as high-z studies have shown gas and Hα having a similar spatial extension (e.g. Molina et al. 2019). The baryonic mass within an $R_{\rm E}$ is simply half the total baryonic mass.

[2] $M_{\rm dyn} = V_{\rm rot}(R_{\rm E})^2\, R_{\rm E}/G$

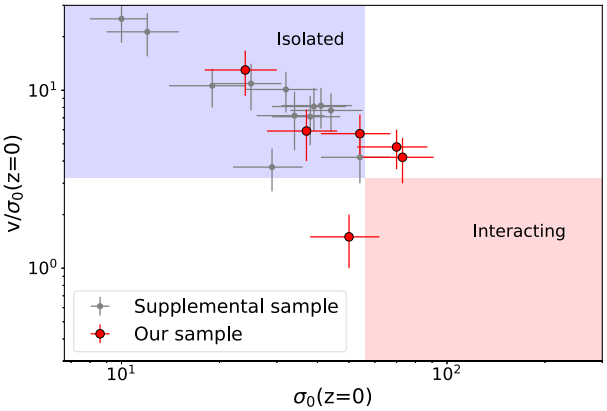

Figure 8. The dynamical ratio for the two sets of luminous IR galaxies: our sample (red) and the supplemental sample (grey). The dynamical ratio has been corrected for the redshift evolution in velocity dispersion as discussed in Section 4.4 The blue/red boxes represent typical values seen in isolated discs/interactions with threshold values of $\sigma_0 < 56$ km s^{-1} and $v_{\rm rot}/\sigma_0 > 3.2$ for isolated discs. 3/6 of our sample appear to be isolated with all 12 of the supplementary sample falling within the boundaries of an isolated galaxy. Galaxies falling within the white areas cannot be determined using this method and can only be categorized by relaxing one of the assumptions.

It is worth noting that the dark matter fractions are subject to large uncertainties due to various assumptions, including uncertainties in the gas fraction, the assumption of the geometry of the mass distribution, assuming the co-spatial distribution of ionized, molecular and stellar mass, and the accuracy of our kinematic parameters recovered from marginally resolved galaxies; and these assumptions are discussed in detail in the KMOS^{3D} (Wuyts et al. 2016) and MOSDEF (Price et al. 2016) kinematic surveys. With all these caveats in mind we can attempt to determine whether both samples as a whole are baryon dominated ($f_{\rm D} < 0.5$) or dark matter dominated ($f_{\rm D} > 0.5$) within their effective radii.

Both samples span a large range of dark matter to dynamical mass fraction, $f_{\rm D}$, from baryon-dominated galaxies to unphysical values. The median value across both samples is $f_{\rm D} = 0.03$ and only three appear to be dark matter dominated within one $R_{\rm E}$ (see Fig. 9), suggesting that high-z luminous IR galaxies are baryon dominated within their effective radii. The ratio of stellar mass to dynamical mass is also plotted in Fig. 9 and contains only two unphysical values, which suggests that the main reason for the unphysical dark matter fractions lies in the estimate for the gas fraction within a galaxy. For example, galaxy o15 lies above the MS so it likely has a lower $\tau_{\rm dep}$ than that acquired from equation (10), which gives a $\tau_{\rm dep}$ of 0.48 Gyr and a gas fraction of 0.87. The $f_{\rm D}$ becomes physical when the gas fraction falls below 0.61.

In the above analysis we included the three galaxies in our KMOS sample (o3, o14, and o16) that failed one of our criteria for an isolated disc. If their high velocity dispersion is due to a perturbation from an interacting galaxy, and the disc has not yet virialized, then equation (6) does not hold. Whether or not we include these three data points the same conclusion holds: we cannot accurately measure the exact $f_{\rm D}$ for an individual galaxy but we can state the sample as a whole is baryon dominated within one $R_{\rm E}$.

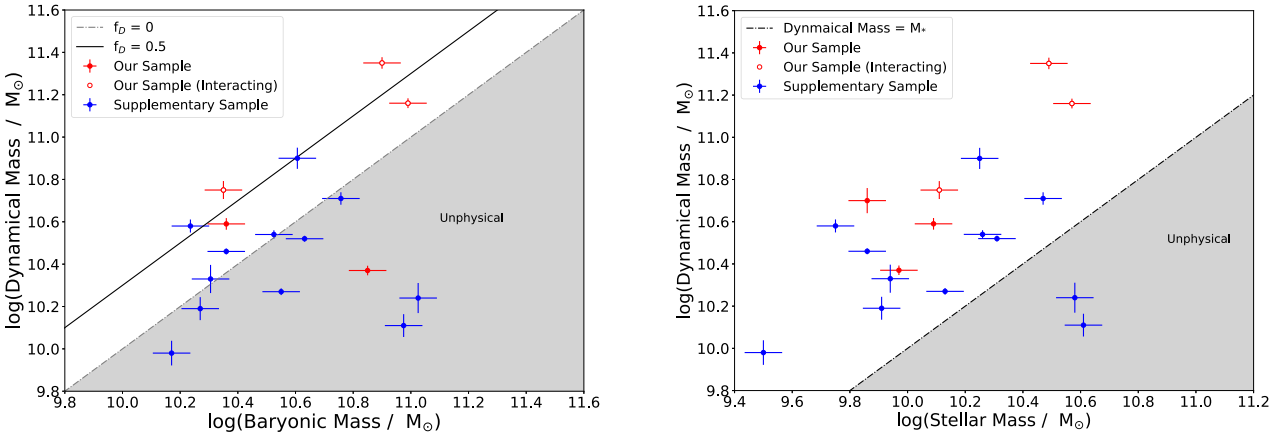

Figure 9. Plot of the dynamical mass versus baryonic mass within one R_E (left) with the grey area representing unphysical values where the baryonic mass exceeds the dynamical mass. Dark matter fraction increases with vertical height above the dashed line, where dynamical mass equals baryonic mass, and the black solid line indicates where the dark matter fraction equals 50 per cent. Three of our sample fall into the dark-matter-dominated region (dark matter fraction $>$ 50 per cent), with eight of our sample in the unphysical region. The unphysical values are mainly caused by our estimate of gas fraction, as discussed in Section 4.5, which can be seen when we remove the gas mass and plot stellar mass versus dynamical mass within one R_E (right). Further reasons for unphyscial values are discussed in Section 4.5. The three galaxies (o3, o14, and o16) that passed only one of our two kinematic criteria for an isolated disc in Section 4.4 are included as the interacting subsample and these may be an overestimate of the dynamical mass. The left plot only contains five data points for our KMOS sample as we were unable to estimate a baryonic mass for galaxy o8.

This agrees with previous high-z research which showed that galactic discs are baryon dominated inside one R_E, displaying a range of median baryon fractions from 70 per cent to unphysical values, i.e. >100 per cent (e.g. Förster Schreiber et al. 2009; Price et al. 2016; Wuyts et al. 2016; Genzel et al. 2017; Lang et al. 2017; Price et al. 2020). Tiley et al. (2019) argued that dark matter fractions of >0.67 are found if f_D is calculated within six radial scale lengths, as opposed to on R_E. All the results are consistent as probing the dark matter fraction at larger radii probes further out into the halo where baryon fraction decreases, assuming a ΛCDM Universe where the universal baryon, Ω_{bar}, to dark matter, Ω_D, fraction is expected to be $f_b = \Omega_{bar}/\Omega_D \sim 0.2$ (Aghanim et al. 2019). Our results are also in agreement with IllustrisTNG simulations where $f_D(<R_E) = 0.29 \pm 0.11$ (Übler et al. 2021) and NewHorizon simulations (Dubois et al. 2020) in which galaxies, similar in SFR to o5 and o16, are baryon dominated within their R_E (Grisdale et al., in preparation).

4.6 Drivers of turbulence

The average velocity dispersion values of the two samples agree within error, but our KMOS sample does appear to have a consistently higher σ_0. Although the supplementary sample satisfy the selection criteria in Section 2.1, these targets were initially selected on their rest-frame optical emission at $2 < z < 2.5$ (Wisnioski et al. 2015), which biases the supplementary sample towards less extinguished objects when compared to our KMOS sample. This leads to a greater S/N in the outer disc regions of the supplementary sample, allowing GalPak^{3D} to probe the kinematics further out into the disc and sample σ_0 away from the central regions of high velocity dispersion.

It is worth investigating potential non-systematic reasons for the range of velocity dispersion within both samples. Previous observational studies (e.g. Johnson et al. 2018; Übler et al. 2019) and semi-analytical modelling (e.g. Krumholz et al. 2018) indicate that turbulence in the high-z Universe is driven primarily by gravitational instability as opposed to feedback from star formation. To check if the σ_0 in our sample is mainly caused by gravitationally unstable discs, we plotted σ_0 versus SFR and versus baryonic mass to try gain insight into the mechanisms driving turbulence. We find weak correlations for σ_0 against baryonic mass with a Pearson's $\rho = 0.37$ (P-value = 0.13), and for σ_0 versus SFR with Pearson's $\rho = 0.30$ (P-value = 0.23), as shown in Fig. 10, although neither is statistically significant. The weak correlation of σ_0 versus SFR may be due to the link between the SFR and baryonic mass, via the main sequence, as opposed to any causal link.

It is also possible that the presence of minor mergers is driving the scatter in dispersion. Such minor merger events could not be observed due to the KMOS being a seeing-limited instrument. Simons et al. (2019) showed, via simulations, that under seeing-limited conditions at $z \sim 2$, mergers can often be mistaken as discs under a variety of sightlines. Fensch et al. (2017) used simulations to demonstrate that mergers at $z \sim 2$ provide an inefficient boost in SFR due to the already turbulent nature of discs at high-z, so being on the MS does not rule out potential mergers. In a forthcoming paper (Hogan et al., in preparation) we will further investigate how minor mergers affect the velocity dispersion within a galaxy and, subsequently, observational signatures such as v_{rot}/σ_0.

4.7 Metallicity

The metal content of a galaxy can be used to constrain its SFH since gas-phase metallicity is the result of enrichment of the ISM from previous star-forming episodes. The ratio of [N II] 6583 Å and Hα, known as the N2 index, can be used to find the gas-phase metal content (Z) of galaxies. We converted the N2 index ratios to 12 + log(O/H) using the correlation of Pettini & Pagel (2004) to compare with the metallicity predicted from the mass–metallicity relation (MZR) at $z \sim 2$. Four of our KMOS sample were marginally detected and their average N2 index is 0.34 ± 0.1. The mean metallicity value derived for our sample is lower than the 1.1 ± 0.8 derived for the intermediate U/LIRG sample (Pereira-Santaella et al. 2019) and the 0.7 ± 0.3 of local U/LIRGs (Rupke,

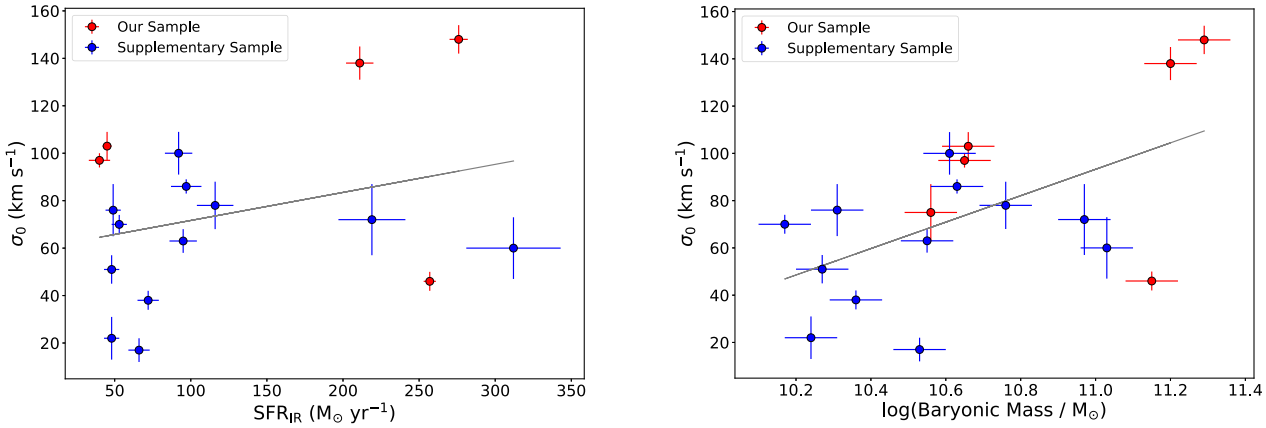

Figure 10. Intrinsic velocity dispersion plotted against SFR (left) and baryonic masses (right) of our galaxies. There is a weak correlation for both σ_0 versus SFR and σ_0 versus baryonic mass with a Pearson's $\rho = 0.37$ (P-value $= 0.23$) and $\rho = 0.37$ (P-value $= 0.13$) for the SFR and baryonic mass, respectively, although neither is statistically significant. Galaxy o8 could not be fitted with an IR SED so we do not have an SFR$_{IR}$ for this galaxy, giving only five data points in our sample for the left plot.

Table 5. The metallicity values of our luminous IR galaxies.

Object	12 + log(O/H)*a*	MZR*b*
o3	8.63 ± 0.12	8.57 ± 0.12
o5	8.60 ± 0.12	8.48 ± 0.14
o7	8.70 ± 0.16	8.52 ± 0.13
o16	8.58 ± 0.13	8.46 ± 0.14
Composite	8.46 ± 0.13	8.52 ± 0.13

Notes.
[a]Metallicity of the galaxy assuming the conversion factor of Pettini & Pagel (2004).
[b]Expected metallicity of the galaxy assuming the MZR of Tacconi et al. (2018).

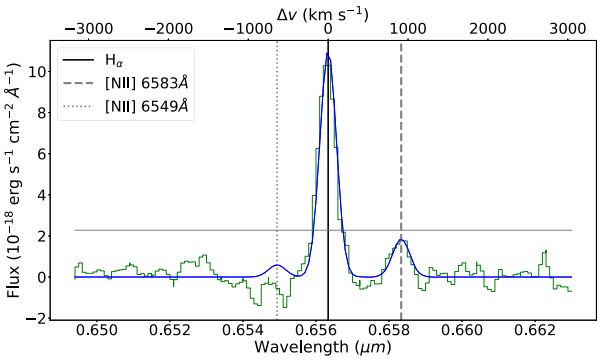

Figure 11. The composite spectra for the eight luminous IR galaxies without detected [N II] 6583 Å emission line. The best-fitting model is overlayed in blue and the vertical solid, dashed, and dotted lines lines represent the position of Hα, [N II] 6549 Å and [N II] 6583 Å lines. This is a marginal $\sim$2.5 σ detection, with the grey horizontal line indicating where S/N $= 3$.

Veilleux & Baker 2008; Alonso-Herrero et al. 2009; Monreal-Ibero et al. 2010), as expected from the redshift evolution of the MZR (e.g. Maiolino et al. 2008).

We can also calculate the expected metallicity of a star-forming galaxy at a given redshift and stellar mass using the following equation from Tacconi et al. (2018):

$$12 + \log(O/H) = a - 0.087 \times (\log M_\star - b)^2, \quad (12)$$

where

$$a = 8.74 \pm 0.06,$$
$$b = 10.4 \pm 0.05 + 4.46 \pm 0.3 \times \log(1+z) - 1.78 \pm 0.4 \times (\log(1+z))^2. \quad (13)$$

Galaxies o3, o5, and o16 all fall close to the expected value of a star-forming galaxy, with galaxy o7 being much more metal enriched than expected, as shown in Table 5 and Figure 12. The N2 index in galaxy o7 falls in a region of the BPT diagram that could be either in the AGN or starburst regime and without the [O III]/Hβ we cannot rule out a deeply buried AGN is skewing the N2 index higher (e.g. Kewley et al. 2013). It is also worth noting that o7 has both the highest Z and highest SFR in our sample which goes against the fundamental metallicity relation (FMR) (e.g.Mannucci et al. 2010; Maiolino & Mannucci 2019), in which for a given stellar mass there is an anticorrelation between SFR and metallicity. Assuming it does not contain an AGN, this galaxy may be a genuine outlier from the FMR or its enhanced Z may be due to different conditions in its ISM, such as an elevated N/O to O/H ratio leading to an error in the N2 to metallicity conversion factor (e.g. Shapley et al. 2015; Dopita et al. 2016). Alternative metallicity diagnostics based on IR fine-structure lines (e.g. Pereira-Santaella et al. 2017; Rigopoulou et al. 2018) may be required to shed light in the metal content of starburst galaxies at high redshifts.

Of the nine targets which had Hα but no [N II] 6583 Å emission, we stacked eight of these targets to try get a detection from a composite spectrum. Galaxy o13 was left out of this stacking as a skyline fell in the same channel as [N II] 6583 Å. We obtained the composite spectrum by shifting the eight spectra into each galaxy's rest frame and then averaged the flux in each channel, which had a bin size of $\sim$1 Å. We fit this spectrum the same three-Gaussian model as the individual galaxies giving a marginal 2.5σ detection, as seen in Fig. 11.

The composite spectra gives an N2 index of 0.17 and 12 + log(O/H) $= 8.46 \pm 0.06$, suggesting that on average these galaxies agree with the MZR at their average redshift of 2.26. The disadvantage of using a stacked spectrum is the average behaviour can hide the underlying variance in the sample, so although the

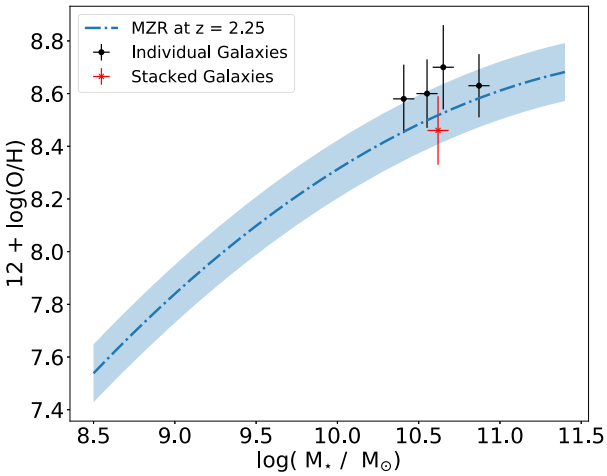

Figure 12. The position of our four galaxies with [N II] 6583 Å detection, and the composite spectrum, with respect to the MZR. The track represents the values expected for z = 2.25 taken from Tacconi et al. (2018), and the scatter in this relation is ∼0.1 dex. This plot indicates our four detections are not metal deficient, with the composite spectrum also lying within the scatter of the MZR.

average metallicity agrees with the MZR this does not rule out a subsample being metal deficient like the local U/LIRGs.

5 CONCLUSION

We performed IFS in a sample of 18 luminous IR galaxies in the redshift range $2 < z < 2.5$, around the peak of cosmic star formation density. We investigated the mechanisms driving their high rates of star formation and compared their properties to local and intermediate-z U/LIRGs to investigate any differences and evolution in the interplay of dust, gas, and star formation between the high-z Universe and today. The main results are:

(i) We detected Hα emission in 14 out of 18 galaxies, with a 3σ upper limit calculated in three of the other four. We fitted an IR SED to 14 of our sample and using the SFRs calculated from the Hα and IR luminosities we show that obscured star formation is an order of magnitude greater than the unobscured star formation within these galaxies. The average obscuration was less than intermediate and local U/LIRGs with $\log(SFR_{H\alpha} / SFR_{IR}) = -1.1 \pm 0.1$.

(ii) 12 of the sample are main-sequence galaxies with two being a starbursts. We determined the distance of each galaxy from the MS, ΔSFR, and found a statistically significant correlation in which $\log(SFR_{H\alpha}/SFR_{IR})$ decreases with increasing ΔSFR, demonstrating obscured star formation increases with distance above the MS.

(iii) Six of our Hα detections converged to a disc within GalPak^{3D}. To boost the sample size we choose a supplementary sample of 28 luminous IR galaxies from the ESO archive, and 12 of this supplemental sample were found to be rotating discs. After accounting for the increase in intrinsic velocity dispersion with lookback time the dynamical ratio (V_{rot}/σ_0) and redshift-corrected σ_0 suggest 15/41, or 17/41 if only $V_{rot}/\sigma_0 > 3.2$ is used, of both samples are isolated discs. This is a higher rate than local and intermediate redshift U/LIRGs, which have ∼5 per cent and ∼25 per cent, respectively. This shows interactions are not necessary to drive the massive SFRs within z ∼ 2 luminous IR galaxies.

(iv) By quantifying the dynamical mass of our galaxies we find them to be baryon dominated inside one R_E, similar to previous studies of star-forming galaxies at z ∼ 2.

(v) FIR photometry allowed us to fit a modified blackbody to seven of our luminous IR galaxies. The dust temperatures fall between 23 and 50 K, in line with dust temperatures in steady-state star-forming galaxies.

(vi) We measured the N2 ratio in four galaxies of our sample. The gas-phase metallicity is in broad agreement with the mass–metallicity relation at z = 2–2.5, in contrast to the metal deficiency of local ULIRGs. For the remaining galaxies in our sample we stacked their spectra allowing a marginal detection of [N II] 6583 Å and average gas-phase metallicity follows the mass–metallicity relation.

In summary, our sample of high-z luminous IR galaxies are predominantly main-sequence star-forming galaxies which have very different behaviour to local U/LIRGs. The underlying mechanisms driving the huge SFRs at the peak of cosmic SFRD are consistent with the steady-state processes driving star-forming disc galaxies we see locally as opposed to mergers.

ACKNOWLEDGEMENTS

We want to thank the anonymous referee for their insightful comments and suggestions that improved the quality of this paper. The analysis in this paper is based on observations made with ESO Telescopes at the La Silla Paranal Observatory under run IDs: 092.B-0769(A) and 097.B-0186(A). D.R., I.G.-B., and K.G. acknowledge support from STFC through grant ST/S000488/1. G.E.M. acknowledges the Villum Fonden research grant 13160 'Gas to stars, stars to dust: tracing star formation across cosmic time' and the Cosmic Dawn Center of Excellence funded by the Danish National Research Foundation under the grant No. 140. N.T. acknowledges support from STFC through grants ST/N002717/1 and ST/S001409/1. M.P.-S. acknowledges support from the Comunidad de Madrid through Atracción de Talento Investigador Grant 2018-T1/TIC-11035.

DATA AVAILABILITY

The data underlying this research are available from the ESO archive (http://archive.eso.org/cms.html) under observation IDs: 200297829-41, 200402165-177 200402203-11.

REFERENCES

Aghanim N. et al., 2019, A&A, 641, A1
Alonso-Herrero A., García-Marín M., Monreal-Ibero A., Colina L., Arribas S., Alfonso-Garzón J., Labiano A., 2009, A&A, 506, 1541
Bauermeister A. et al., 2013, ApJ, 768, 132
Bellocchi E., Arribas S., Colina L., Miralles-Caballero D., 2013, A&A, 557, A59
Bellocchi E., Arribas S., Colina L., 2016, A&A, 591, A85
Bertelli G., Bressan A., Chiosi C., Fagotto F., Nasi E., 1994, A&AS, 106, 275
Béthermin M. et al., 2015, A&A, 573, A113
Bolatto A. D., Wolfire M., Leroy A. K., 2013, ARA&A, 51, 207
Bouché N., Carfantan H., Schroetter I., Michel-Dansac L., Contini T., 2015, AJ, 150, 92
Bruzual G., Charlot S., 2003, MNRAS, 344, 1000
Buat V. et al., 2015, A&A, 577, A141
Buat V., Ciesla L., Boquien M., Malek K., Burgarella D., 2019, A&A, 632, A79
Calzetti D., Armus L., Bohlin R. C., Kinney A. L., Koornneef J., Storchi-Bergmann T., 2000, ApJ, 533, 682
Casey C. M., Narayanan D., Cooray A., 2014, Phys. Rep., 541, 45
Chabrier G., 2003, PASP, 115, 763
Chen Z., Fang G., Lin Z., Zhang H., Chen G., Kong X., 2021, ApJ, 906, 71
Chomiuk L., Povich M. S., 2011, AJ, 142, 197

Clements D. L. et al., 2018, MNRAS, 475, 2097
Combes F., 2018, A&AR, 26, 5
Cortese L. et al., 2014, MNRAS, 440, 942
D'Amato Q. et al., 2020, A&A, 636, A37
Daddi E. et al., 2007, ApJ, 670, 156
Daddi E. et al., 2010a, ApJ, 713, 686
Daddi E. et al., 2010b, ApJ, 714, L118
Davies R. I. et al., 2013, A&A, 558, A56
Dekel A., Burkert A., 2014, MNRAS, 438, 1870
Dekel A., Sari R., Ceverino D., 2009, ApJ, 703, 785
Díaz-Santos T. et al., 2017, ApJ, 846, 32
Dopita M. A., Kewley L. J., Sutherland R. S., Nicholls D. C., 2016, Ap&SS, 361, 61
Dowell C. D. et al., 2013, ApJ, 780, 75
Draine B. T., Li A., 2007, ApJ, 657, 810
Drew P. M., Casey C. M., Cooray A., Whitaker K. E., 2020, ApJ, 892, 104
Dubois Y. et al., 2020, preprint (arXiv:2009.10578 [astro-ph])
Elbaz D. et al., 2011, A&A, 533, A119
Elbaz D. et al., 2018, A&A, 616, A110
Elmegreen B. G., Elmegreen D. M., 2006, ApJ, 650, 644
Fan L., Jones S. F., Han Y., Knudsen K. K., 2017, PASP, 129, 124101
Farrah D. et al., 2008, ApJ, 677, 957
Fensch J. et al., 2017, MNRAS, 465, 1934
Floc'h E. L. et al., 2005, ApJ, 632, 169
Förster Schreiber N. M. et al., 2009, ApJ, 706, 1364
Franco M. et al., 2018, A&A, 620, A152
Franco M. et al., 2020, A&A, 643, A30
Freudling W., Romaniello M., Bramich D. M., Ballester P., Forchi V., García-Dabló C. E., Moehler S., Neeser M. J., 2013, A&A, 559, A96
Gao Y., Solomon P. M., 2004, ApJ, 606, 271
Genzel R. et al., 2010, MNRAS, 407, 2091
Genzel R. et al., 2015, ApJ, 800, 20
Genzel R. et al., 2017, Nature, 543, 397
Graciá-Carpio J. et al., 2011, ApJ, 728, L7
Hodge J. A. et al., 2019, ApJ, 876, 130
Hopkins A. M., Connolly A. J., Haarsma D. B., Cram L. E., 2001, AJ, 122, 288
Huang J.-S. et al., 2014, ApJ, 784, 52
Iono D. et al., 2009, ApJ, 695, 1537
Johnson H. L. et al., 2018, MNRAS, 474, 5076
Kartaltepe J. S. et al., 2012, ApJ, 757, 23
Kennicutt R. C., 1998, ARA&A, 36, 189
Kennicutt R. C., Evans N. J., 2012, ARA&A, 50, 531
Kewley L. J., Dopita M. A., Leitherer C., Davé R., Yuan T., Allen M., Groves B., Sutherland R., 2013, ApJ, 774, 100
Krajnović D., Cappellari M., de Zeeuw P. T., Copin Y., 2006, MNRAS, 366, 787
Kriek M. et al., 2015, ApJS, 218, 15
Kroupa P., 2001, MNRAS, 322, 231
Krumholz M. R., Burkhart B., Forbes J. C., Crocker R. M., 2018, MNRAS, 477, 2716
Lang P. et al., 2017, ApJ, 840, 92
Larson K. L. et al., 2016, ApJ, 825, 128
Madau P., Dickinson M., 2014, ARA&A, 52, 415
Magdis G. E. et al., 2010, MNRAS, 409, 22
Magdis G. E. et al., 2012, ApJ, 760, 6
Magdis G. E. et al., 2013, A&A, 558, A136
Magdis G. E. et al., 2014, ApJ, 796, 63
Magnelli B. et al., 2014, A&A, 561, A86
Magnelli B., Elbaz D., Chary R. R., Dickinson M., Borgne D. L., Frayer D. T., Willmer C. N. A., 2011, A&A, 528, A35
Maiolino R. et al., 2008, A&A, 488, 463
Maiolino R., Mannucci F., 2019, A&AR, 27, 3
Mannucci F., Cresci G., Maiolino R., Marconi A., Gnerucci A., 2010, MNRAS, 408, 2115
Martin G., Kaviraj S., Devriendt J. E. G., Dubois Y., Laigle C., Pichon C., 2017, MNRAS, 472, L50
Miettinen O. et al., 2017, A&A, 606, A17
Miller S. H., Bundy K., Sullivan M., Ellis R. S., Treu T., 2011, ApJ, 741, 115
Molina J., Ibar E., Swinbank A. M., Sobral D., Best P. N., Smail I., Escala A., Cirasuolo M., 2017, MNRAS, 466, 892
Molina J., Ibar E., Smail I., Swinbank A. M., Villard E., Escala A., Sobral D., Hughes T. M., 2019, MNRAS, 487, 4856
Monreal-Ibero A., Arribas S., Colina L., Rodríguez-Zaurín J., Alonso-Herrero A., García-Marín M., 2010, A&A, 517, A28
Murphy E. J. et al., 2011b, ApJ, 737, 67
Murphy E. J., Chary R.-R., Dickinson M., Pope A., Frayer D. T., Lin L., 2011a, ApJ, 732, 126
Muzzin A., van Dokkum P., Kriek M., Labbé I., Cury I., Marchesini D., Franx M., 2010, ApJ, 725, 742
Noeske K. G. et al., 2007, ApJ, 660, L43
Osterbrock D. E., Ferland G. J., 2006, in Osterbrock D. E., Ferland G. J., eds, Astrophysics of Gaseous Nebulae and Active Galactic Nuclei, 2nd. ed., University Science Books, Sausalito, CA
Pereira-Santaella M. et al., 2018, A&A, 616, A171
Pereira-Santaella M. et al., 2019, MNRAS, 486, 5621
Pereira-Santaella M., Rigopoulou D., Farrah D., Lebouteiller V., Li J., 2017, MNRAS, 470, 1218
Pettini M., Pagel B. E. J., 2004, MNRAS, 348, L59
Pettini M., Shapley A. E., Steidel C. C., Cuby J.-G., Dickinson M., Moorwood A. F. M., Adelberger K. L., Giavalisco M., 2001, ApJ, 554, 981
Piotrowska J., Bluck A. F. L., Maiolino R., Concas A., Peng Y., 2019, MNRAS, 492, L6
Popping G. et al., 2017, A&A, 602, A11
Price S. H. et al., 2016, ApJ, 819, 80
Price S. H. et al., 2020, ApJ, 894, 91
Rigopoulou D. et al., 2014, ApJ, 781, L15
Rigopoulou D., Lawrence A., Rowan-Robinson M., 1996, MNRAS, 278, 1049
Rigopoulou D., Pereira-Santaella M., Magdis G. E., Cooray A., Farrah D., Marques-Chaves R., Perez-Fournon I., Riechers D., 2018, MNRAS, 473, 20
Rodighiero G. et al., 2011, ApJ, 739, L40
Rodrigues M., Hammer F., Flores H., Puech M., Athanassoula E., 2017, MNRAS, 465, 1157
Rodríguez-Zaurín J., Arribas S., Monreal-Ibero A., Colina L., Alonso-Herrero A., Alfonso-Garzón J., 2011, A&A, 527, A60
Rodríguez Montero F., Davé R., Wild V., Anglés-Alcázar D., Narayanan D., 2019, MNRAS, 490, 2139
Rupke D. S. N., Veilleux S., Baker A. J., 2008, ApJ, 674, 172
Saintonge A. et al., 2013, ApJ, 778, 2
Sanders D. B., Mirabel I. F., 1996, ARA&A, 34, 749
Sargent M. T., Béthermin M., Daddi E., Elbaz D., 2012, ApJ, 747, L31
Schmidt M., 1959, ApJ, 129, 243
Scoville N. et al., 2016, ApJ, 820, 83
Scoville N. et al., 2017, ApJ, 837, 150
Shapley A. E. et al., 2015, ApJ, 801, 88
Sharples R. et al., 2013, The Messenger, 151, 21
Simons R. C. et al., 2016, ApJ, 830, 14
Simons R. C. et al., 2019, ApJ, 874, 59
Speagle J. S., Steinhardt C. L., Capak P. L., Silverman J. D., 2014, ApJS, 214, 15
Stott J. P. et al., 2016, MNRAS, 457, 1888
Straatman C. M. S. et al., 2016, ApJ, 830, 51
Symeonidis M., Page M. J., 2018, MNRAS, 479, L91
Tacconi L. J. et al., 2008, ApJ, 680, 246
Tacconi L. J. et al., 2013, ApJ, 768, 74
Tacconi L. J. et al., 2018, ApJ, 853, 179
Tacconi L. J., Genzel R., Sternberg A., 2020, ARA&A, 58, null
Tiley A. L. et al., 2019, MNRAS, 485, 934
Turner O. J. et al., 2017, MNRAS, 471, 1280
Valentino F. et al., 2020, A&A, 641, A155
Wegner M., Muschielok B., 2008, in Bridger A., Radziwill N. M., eds, Proc. SPIE Conf. Ser. Vol. 7019, Advanced Software and Control for Astronomy II. SPIE, Bellingham, p. 70190T
Whitaker K. E. et al., 2014, ApJ, 795, 104

Whitaker K. E., Dokkum P. G. V., Brammer G., Franx M., 2012, ApJ, 754, L29
Wiklind T. et al., 2019, ApJ, 878, 83
Wisnioski E. et al., 2015, ApJ, 799, 209
Wisnioski E. et al., 2019, ApJ, 886, 124
Wuyts S. et al., 2016, ApJ, 831, 149
Übler H. et al., 2019, ApJ, 880, 48
Übler H. et al., 2021, MNRAS, 500, 4597

APPENDIX A: SUPPLEMENTARY SAMPLE

Table A1. Supplementary sample of luminous IR galaxies selected from the archive.

ZFOURGE ID	KMOS^{3D} ID	RA deg	Dec. deg	z	log(M$_\star$)[a] M$_\odot$	SFR$_{H\alpha}$[b] M$_\odot$ yr^{-1}	SFR$_{IR}$[c] M$_\odot$ yr^{-1}
25940	GS4 1748	53.101	−27.716	2.301	10.78	14	45
24313	GS4 38560	53.078	−27.731	2.417	10.21	13	48
19322	GS4 30548	53.078	−27.772	2.113	10.05	20	48
23965	GS4 37988	53.052	−27.734	2.201	10.24	13	49
24103	GS4 38116	53.171	−27.733	2.197	10.20	19	52
18414	GS4 28870	53.182	−27.780	2.471	9.82	21	52
28441	GS4 46432	53.112	−27.693	2.435	9.80	46	53
25583	GS4 40768	53.041	−27.719	2.303	10.14	71	61
24415	GS4 38807	53.182	−27.730	2.318	10.22	15	61
21242	GS4 33639	53.121	−27.756	2.235	10.56	19	66
26243	GS4 42235	53.135	−27.713	2.433	10.16	51	72
6000	GS4 05979	53.135	−27.882	2.393	10.28	16	75
9927	GS4 14070	53.229	−27.846	2.306	10.44	21	90
10521	GS4 15000	53.116	−27.842	2.035	10.55	15	92
22233	GS4 35056	53.168	−27.749	2.227	10.43	14	95
26492	GS4 42789	53.034	−27.711	2.254	10.61	39	97
17344	GS4 27404	53.072	−27.786	2.035	10.49	32	108
27238	GS4 44133	53.110	−27.704	2.140	10.77	21	116
23812	GS4 37745	53.183	−27.735	2.431	10.91	27	129
16282	GS4 25151	53.100	−27.794	2.223	10.59	35	130
10780	GS4 15819	53.180	−27.839	2.042	10.59	17	131
27751	GS4 45188	53.063	−27.700	2.406	10.72	15	173
25918	GS4 41438	53.019	−27.717	2.018	10.46	22	189
25326	GS4 40477	53.054	−27.722	2.061	10.91	16	219
26148	GS4 42127	53.051	−27.714	2.442	10.88	29	312
19033	GS4 30274	53.131	−27.773	2.225	11.17	65	512
25730	GS4 41181	53.107	−27.718	2.300	11.06	5	776
2466	GS4 01529	53.180	−27.921	2.122	11.30	44	782

Notes.
[a]Stellar mass of the galaxy. We assume an error of 15% in any calculation that required the stellar mass.
[b]SFRs calculated from the Hα luminosity from the KMOS^{3D} catalogue (Wisnioski et al. 2019).
[c]SFRs calculated from the IR luminosity from ZFOURGE (Straatman et al. 2016).

Table A2. Kinematic parameters of the best-fitting model galaxy from GalPak^{3D} for the supplementary sample of luminous IR galaxies.

ID	R_E[a] kpc	i[b] deg	PA[c] deg	v_{max}[d] km s^{-1}	σ_0[e] km s^{-1}	$\sigma_0(z=0)$[f] km s^{-1}	f_{gas}[g]	$v_{rot}/\sigma_0(z=0)$[h]	$\log(M_{dyn})$[i] $M_\odot$	M_{bar}/M_{dyn}[j]
GS4 38560	2.76 ± 0.31	48 ± 7	78 ± 6	274 ± 46	51 ± 6	25 ± 6	0.56	10.90 ± 3.24	10.19 ± 0.05	1.21 ± 0.20
GS4 30548	2.76 ± 0.18	26 ± 3	323 ± 4	247 ± 28	22 ± 9	12 ± 3	0.67	21.33 ± 5.77	10.58 ± 0.03	0.45 ± 0.17
GS4 37988	1.97 ± 0.30	82 ± 7	52 ± 8	318 ± 35	76 ± 11	39 ± 10	0.57	8.11 ± 2.18	10.33 ± 0.07	0.94 ± 0.21
GS4 46432	1.32 ± 0.03	15 ± 2	350 ± 7	249 ± 64	70 ± 4	34 ± 8	0.79	7.25 ± 2.58	9.98 ± 0.06	1.55 ± 0.20
GS4 33639	3.36 ± 0.13	32 ± 3	274 ± 2	252 ± 27	17 ± 5	10 ± 2	0.46	25.20 ± 6.75	10.54 ± 0.02	0.97 ± 0.16
GS4 42235	3.00 ± 0.10	62 ± 2	127 ± 1	198 ± 8	38 ± 4	19 ± 5	0.69	10.61 ± 2.64	10.46 ± 0.01	0.79 ± 0.15
GS4 15000	5.18 ± 0.57	76 ± 7	16 ± 4	227 ± 30	100 ± 9	54 ± 13	0.56	4.24 ± 1.18	10.90 ± 0.05	0.51 ± 0.15
GS4 35056	1.37 ± 0.05	50 ± 3	1 ± 1	328 ± 20	63 ± 5	32 ± 8	0.62	10.15 ± 2.57	10.27 ± 0.02	1.91 ± 0.15
GS4 42789	2.60 ± 0.08	31 ± 3	42 ± 4	337 ± 18	86 ± 3	44 ± 11	0.52	7.68 ± 1.93	10.52 ± 0.01	1.29 ± 0.15
GS4 44133	2.76 ± 0.18	32 ± 5	268 ± 6	335 ± 28	78 ± 10	41 ± 10	0.49	8.21 ± 2.13	10.71 ± 0.03	1.12 ± 0.16
GS4 40477	1.50 ± 0.15	56 ± 13	160 ± 97	271 ± 52	72 ± 15	38 ± 9	0.57	7.07 ± 2.20	10.11 ± 0.05	7.28 ± 0.19
GS4 42127	2.53 ± 0.41	84 ± 7	79 ± 5	110 ± 14	60 ± 13	29 ± 7	0.64	3.74 ± 1.03	10.24 ± 0.07	6.16 ± 0.22

Notes.
[a]Half-light radius of Hα emission assuming an exponential Sersic profile.
[b]Galaxy inclination.
[c]Position angle east of north to the blue-shifted major kinematic axis.
[d]De-projected maximum velocity of the asymptotically flat part of the rotation curve.
[e]Intrinsic velocity dispersion of galaxy disc.
[f]The expected velocity dispersion of the galaxy at z = 0 assuming the redshift evolution of velocity dispersion. See Section 4.4.
[g]Estimated gas fraction of the galaxy. See Section 4.5.
[h]The dynamical ratio of the galaxy assuming the corrected velocity dispersion at z = 0.
[i]Dynamical mass of the galaxy. See Section 9.
[j]Fraction of the total galaxy mass comprised of baryonic matter. See Section 4.5.

APPENDIX B: KINEMATICS

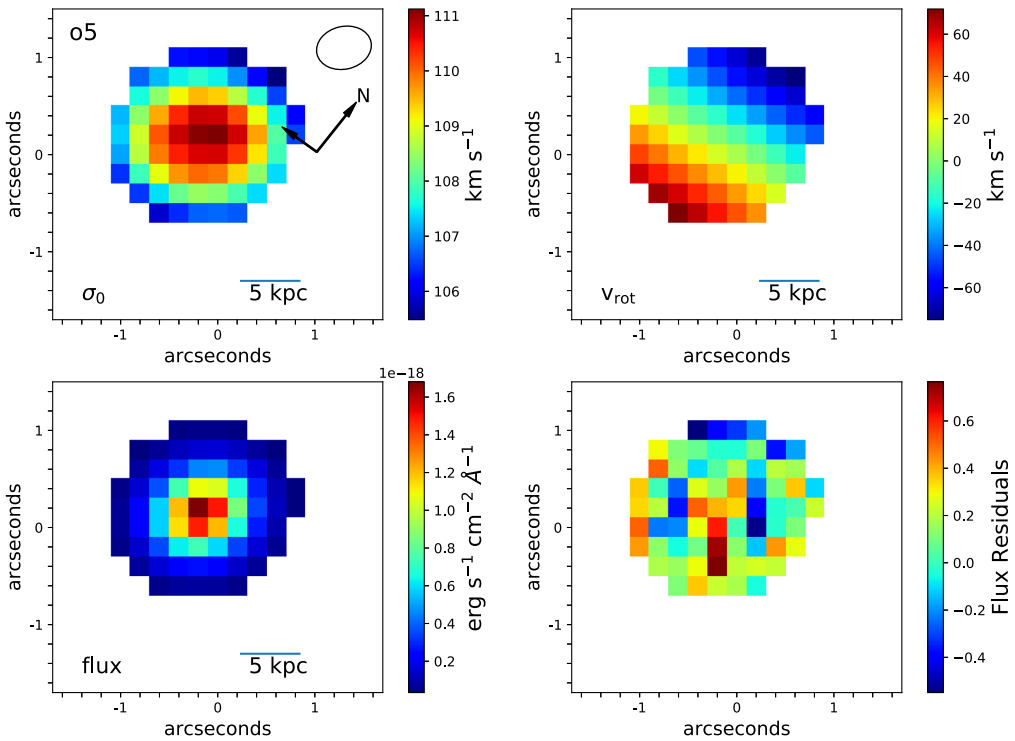

Figure B1. Same as Figure 3 except for galaxy o5.

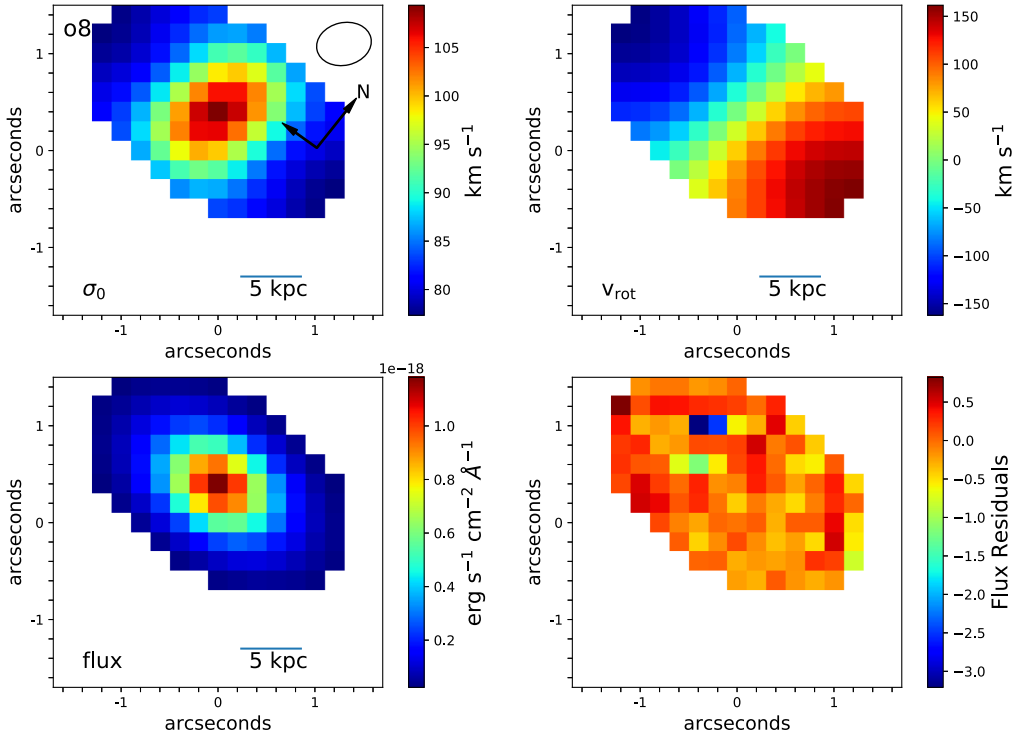

Figure B2. Same as Figure 3 except for galaxy o8.

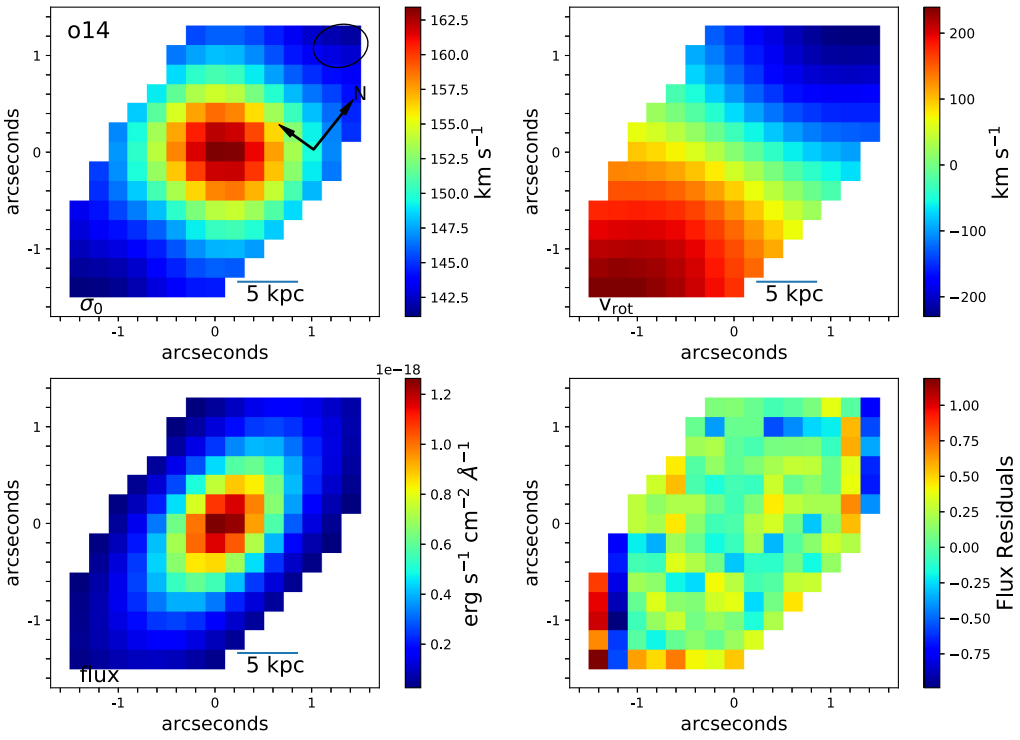

Figure B3. Same as Figure 3 except for galaxy o14.

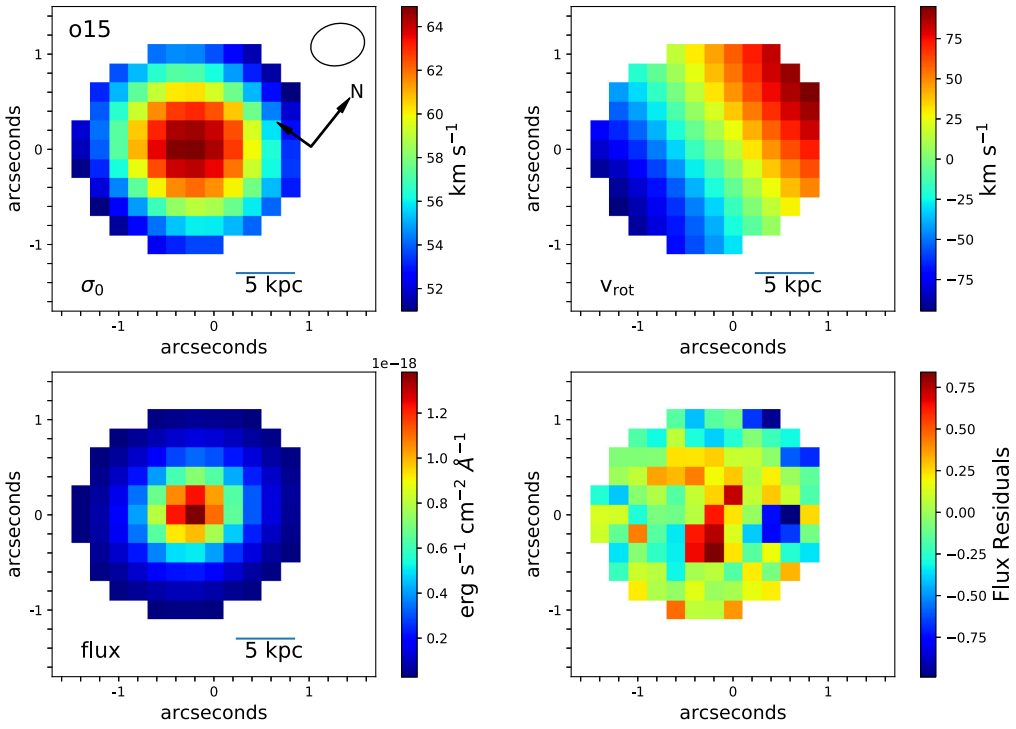

Figure B4. Same as Figure 3 except for galaxy o15.

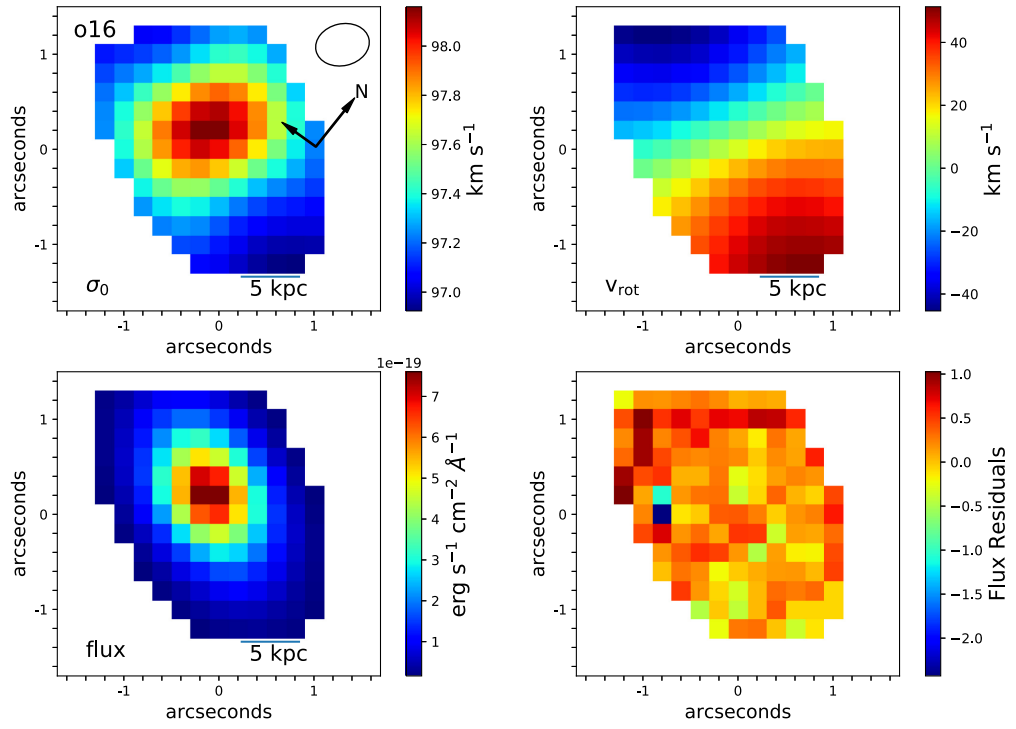

Figure B5. Same as Figure 3 except for galaxy o16.

APPENDIX C: *HST* ACS IMAGES

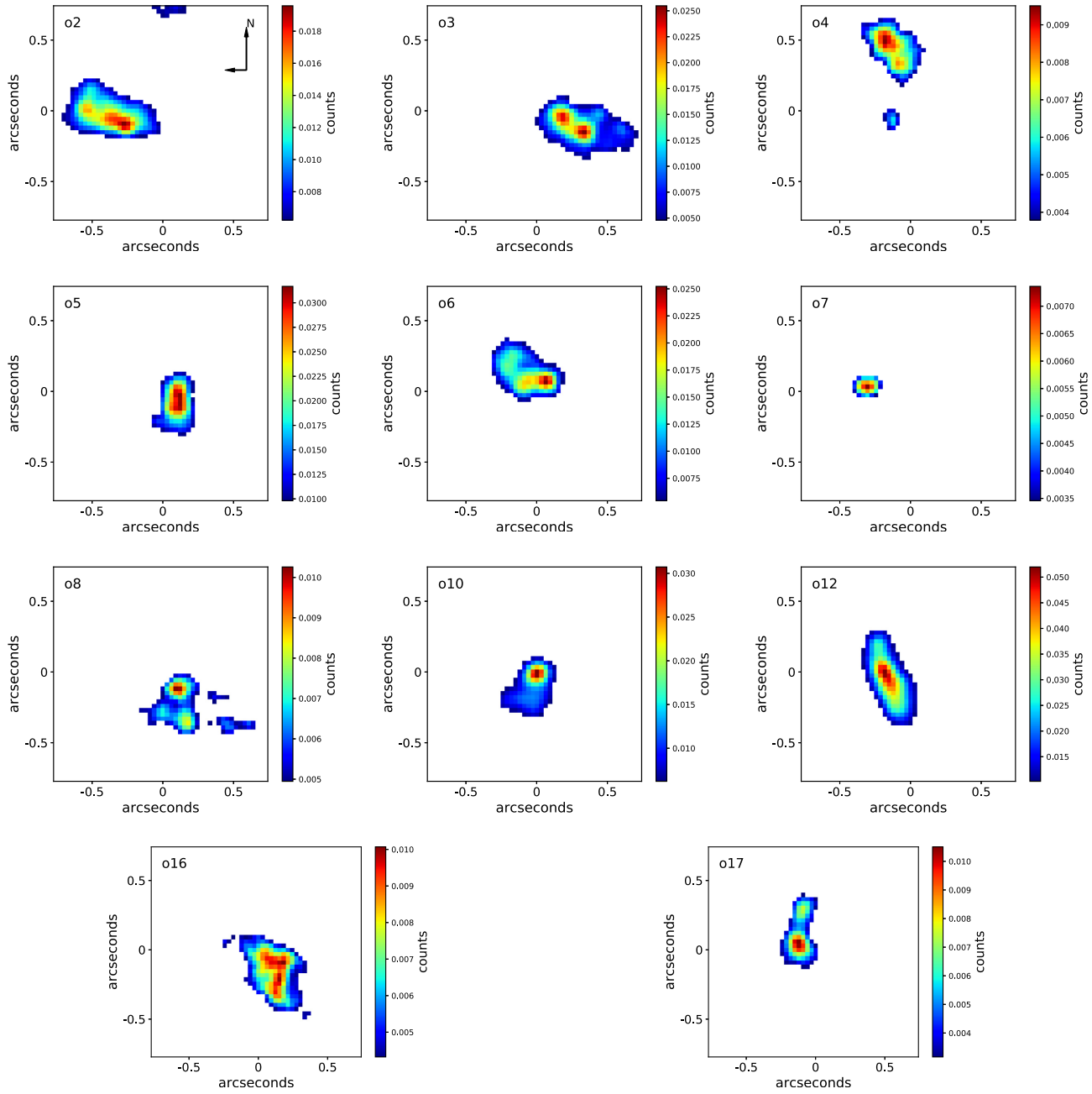

Figure C1. Broad-band images from the ACS/WFC F814W filter on board the *Hubble Space Telescope*, with a 3σ threshold, and centred on the coordinates in Table 1. Three of our KMOS galaxies with Hα detections, o13, o14, and o15, have not been included due to poor S/N.

APPENDIX D: MODIFIED BLACKBODY

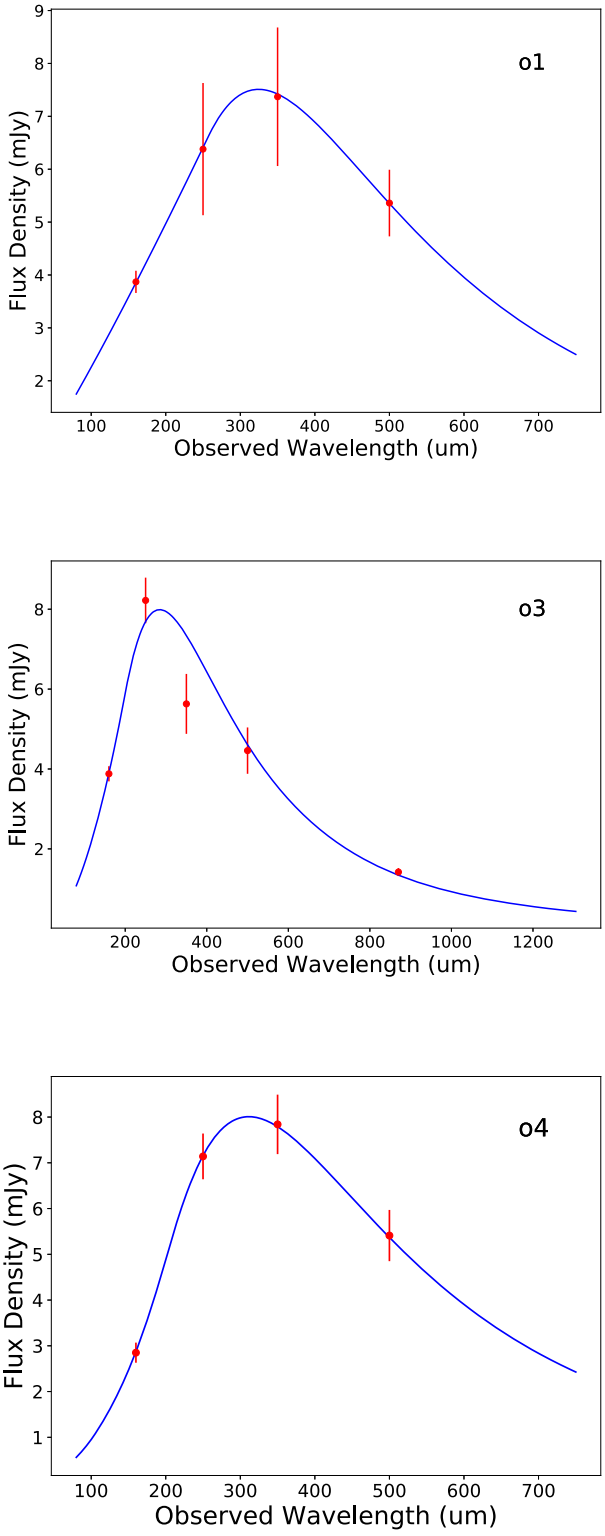

Figure D1. Modified blackbodies, as described in Section 4.3, fitted to the galaxies in our KMOS sample which have three or more photometry points $>100\mu$m. The best fit from the MCMC is plotted in blue and the observed flux is given by the red data points.

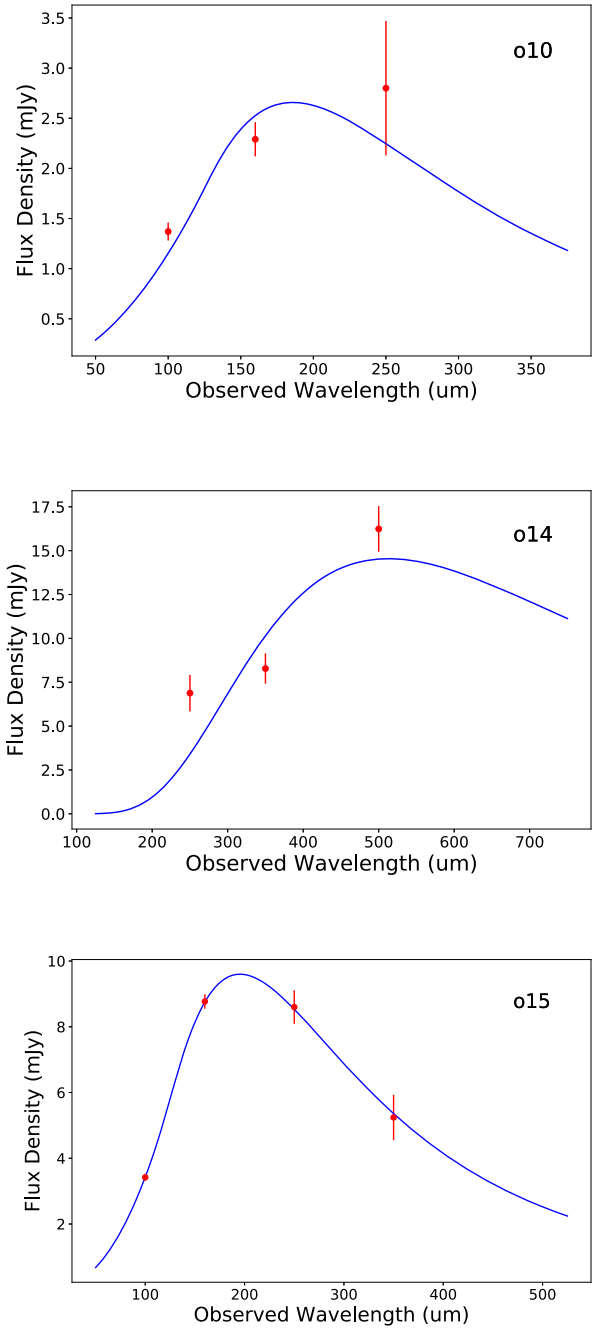

Figure D1 continued.

This paper has been typeset from a TEX/LATEX file prepared by the author.